FERMILAB-Pub-03/330 October 2003

Dark current, breakdown, and magnetic field effects in a multicell, 805 MHz cavity

J. Norem
HEP Division, Argonne National Laboratory, Argonne, Illinois 60439, USA

V. Wu*
University of Cincinnati, Cincinnati, Ohio 45221, USA

A. Moretti, M. Popovic, and Z. Qian
Fermi National Accelerator Laboratory, Batavia, Illinois 60510, USA

L. Ducas
University of Illinois, Urbana, Illinois 61801, USA

Y. Torun and N. Solomey
Illinois Institute of Technology, Chicago, Illinois 60616, USA
(Received 22 April 2002; revised manuscript received 9 January 2003; published 30 July 2003; publisher error corrected 15 August 2003)

We present measurements of dark currents and x rays in a six cell 805 MHz cavity, taken as part of an rf development program for muon cooling, which requires high power, high stored energy, low frequency cavities operating in a strong magnetic field. We have done the first systematic study of the behavior of high power rf in a strong (2.5–4 T) magnetic field. Our measurements extend over a very large dynamic range in current and provide good fits to the Fowler-Nordheim field emission model assuming mechanical structures produce field enhancements at the surface. The locally enhanced field intensities we derive at the tips of these emitters are very large, (~10 GV/m), and should produce tensile stresses comparable to the tensile strength of the copper cavity walls and should be capable of causing breakdown events. We also compare our data with estimates of tensile stresses from a variety of accelerating structures. Preliminary studies of the internal surface of the cavity and window are presented, which show splashes of copper with many sharp cone shaped protrusions and wires which can explain the experimentally measured field enhancements. We discuss a "cold copper" breakdown mechanism and briefly review alternatives. We also discuss a number of effects due to the 2.5 T solenoidal fields on the cavity such as altered field emission due to mechanical deformation of emitters, and dark current ring beams, which are produced from the irises by $E \times B$ drifts during the non-relativistic part of the acceleration process.

PACS numbers: 29.17.+w, 52.80.Vp

I. INTRODUCTION

The problem of operating single particle detectors in the presence of rf cavities, with the immediate goal of an experimental demonstration of muon cooling, has directed interest at the study of dark currents and the x rays they produce. There has been work on maintaining high electric fields in vacuum for the last 100 years, and this effort is summarized in a number of recent books [1–6], theses [7–9], and papers [10,11].

Our goal is to develop high gradient 200 MHz cavities suitable for muon cooling, and the primary problem is the emission of dark currents which cause backgrounds in our detectors and breakdown in the cavities. While dark current phenomena are almost universally seen in accelerating structures, there has been comparatively little systematic study with low frequency copper accelerating structures operating in a strong magnetic field. We used an 805 MHz cavity (Fig. 1) to help understand the phenomena involved in dark current emission and transport [12,13]. The accelerating field for this π-mode cavity is given by $E_{acc,[\mathrm{MV/m}]} = \sqrt{33P_{[\mathrm{MW}]}}$, and the maximum surface field is 2.6 times E_{acc}. The maximum power available was about 14 MW.

This cavity was designed to accelerate muons between absorbers in a muon cooling channel [14–16]. Since cooling cell designs require high gradient rf within strong solenoidal magnetic fields, the test cell is surrounded by a two coil superconducting magnet capable of producing either a solenoidal mode, with the coils in series adding, or a gradient mode, with the coils in opposition. The magnet can produce a 5 T field on axis in the solenoidal mode, and in gradient mode the field flips from +3.5 to −3.5 T [17].

This paper presents measurements of dark currents and related effects over a wide range of accelerating fields and currents and compares the results with simple models. These measurements of field emission with high power rf

*Now at Fermilab, Batavia, IL, USA.

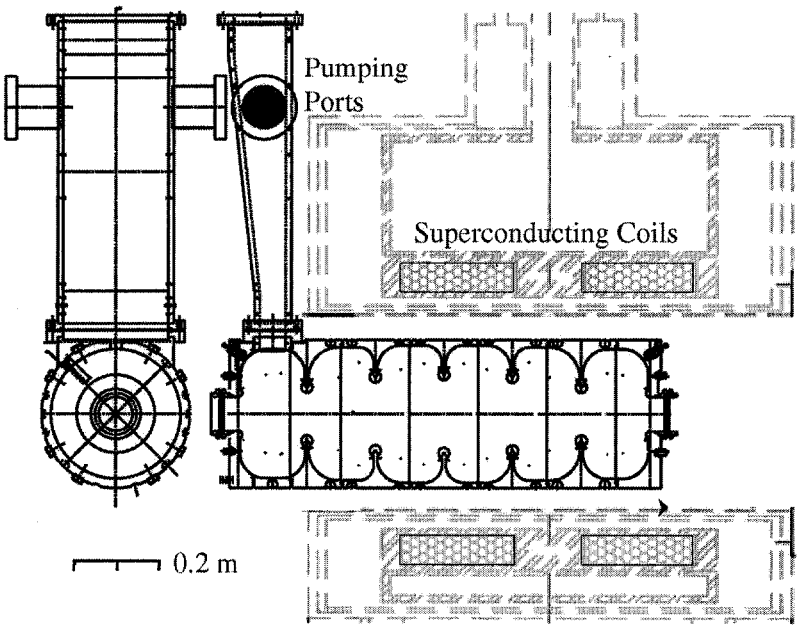

FIG. 1. (Color) The rf cavity in the superconducting magnet.

in a high magnetic field are the first systematic study of this effect. The Fowler-Nordheim field emission model [18] is the simplest process involved, but not the only one, and the idea of large enhancements produced by mechanical structures is not universally accepted [5,19].

We have fit field emission data using two parameters which produce estimates of the emitter area and field enhancement, and shown that the molten copper splashes inside the cavity display structures which have the approximate areas and shapes predicted by our dark current data. We estimated the emitter density by looking at the dark current beamlets produced when the solenoidal field was turned on. Closer study of these beamlets showed that under some conditions these beamlets formed rings, which we have explained as a result of transverse momentum imparted to the electrons by $\mathbf{E} \times \mathbf{B}$ drifts during the nonrelativistic part of the acceleration. We also describe how magnetic fields interact mechanically with emitter structures.

We find that breakdown can be explained by a combination of the electromagnetic stress, the mechanical structures we observe on the surface, and the tensile strength of the material [20,21]. We describe the phenomenon, show how it can produce breakdown, and use a variety of new data to study operating conditions of existing facilities. A wide variety of other cavity measurements (vacuum, pulse length, etc.) seem to be consistent with this model.

II. DARK CURRENT SOURCES

Fowler-Nordheim field emission, which proceeds by quantum tunneling through a potential barrier, is described by a current density, $i(E)$, in A/m^2 given by [1,22]

$$i(E_{\mathrm{surf}}) = \frac{A_{\mathrm{FN}}(\beta E_{\mathrm{surf}})^2}{\phi} \exp\left(-\frac{B_{\mathrm{FN}}\phi^{3/2}}{\beta E_{\mathrm{surf}}}\right),$$

where E_{surf} is the surface electric field on the irises, in MV/m, ϕ is the work function of the material in eV, with $A_{\mathrm{FN}} = 1.54 \times 10^6$ eV A/(MV)^2, $B_{\mathrm{FN}} = 6830$ MV/m(eV)$^{3/2}$, and β is the ratio of the local electric field at the presumably pointlike emitter, to the average surface field [1,18,22]. The accelerating field, E_{acc}, the total field enhancement, β_{tot}, and the local field at the emitter tips, E, are defined by the relation $\beta_{\mathrm{tot}}E_{\mathrm{acc}} = \beta E_{\mathrm{surf}} = E$. For all useful materials the work function is approximately 4.6 eV. We assume the emitted current is then $I(E) = A_{\mathrm{rf}}A_e i(E)$, where A_e is the total emitter area, and A_{rf}, described below, corrects for the time variation of the sinusoidal field. The term A_{rf} is essentially the duty cycle of the emitter, which is active only for a small fraction of the rf pulse. This term is evaluated in Sec. V and found to be equal to about 0.1. We plot $\log_{10}I$ vs $\log_{10}E_{\mathrm{acc}}$, which presents the data as a function of the measurable quantities, where the effects of the two variables, β and A_e, are simple and comparatively intuitive. This format also permits comparisons between data from different facilities and detectors, and can show perturbations, for example, due to the $I \sim E^{3/2}$ dependence of space charge limited currents. The structure of the data makes relatively precise measurements of β possible, but the experimental errors in determining A_e are comparatively large.

We assume that emission from a cavity is dominated by emitters whose local electric field is in the range 1–10 GV/m. This is because the rapid rise of current with field heavily weights the data towards the highest field emitters. We measure the sum of currents from different emitters in the cavity in a somewhat imprecise way, detecting only the fraction of the current which is emitted through the window. The total field enhancement, $\beta_{\rm tot}$ is expected to be due to a number of factors: (i) the shape of the cavity makes the local field on the irises higher by a factor of about 2.6; (ii) visible roughness such as pitting, scratches, and copper beads deposited from breakdown will produce an additional factor, probably around 5; and (iii) the actual emitter point seems to be sharp, considerably smaller than 1 μm, contributing another factor of perhaps 20–30. These factors are multiplied together to give the observed enhancement.

While large enhancement factors could be a function of the product of many smaller enhancements, they could be produced by single structures. For example it has been shown that a hairlike metallic protrusion with a length N times its diameter and a spherical end whose radius is equal to that of the hair would produce an enhancement factor roughly equal to N [19]. While these structures seem unlikely, we did see metallic hairs lying down on the surface with comparable dimensions. These hairs are described below, along with mechanisms which can stand them on end.

There are other electron emission mechanisms in addition to Fowler-Nordheim tunneling, such as thermal emission, plasma effects, etc. [1]. Thermal emission is described by the expression

$$i_{\rm th}(T) = AT^2 e^{-\phi/k_B T},$$

where A is equal to 1.2×10^6 A/m^2 K^2, k_B is Boltzmann's constant, equal to 8.62×10^6 eV/K, T is the temperature, and ϕ is the work function of a few eV [23]. The expressions for thermal emission and tunneling are qualitatively similar. Unless the emitter temperature is above 5000 K, however, thermal emission current is many orders of magnitude lower than the current density from Fowler-Nordheim tunneling. Nevertheless, thermal emission may be involved more directly in breakdown, where very high densities of local heating may be found.

III. CAVITY MEASUREMENTS

A. $B_{\rm sol} = 0$

The conditioning of the cavity (described below) involved operating it at the highest possible accelerating gradient for about 6 weeks. The study of dark currents began in the middle of the conditioning procedure, with measurements using a beam transformer that was read out with a Tektronix TDS 3054 oscilloscope [24,25]. As the conditioning progressed, we extended the lower limit of current measurements by averaging up to 64 pulses to suppress high frequency noise from the signal. Towards the end of the measurements, we also used a 100× rf amplifier with a high frequency cutoff around 10 MHz, mounted near the transformer, to improve the signal to noise ratio and permit more accurate measurements with smaller currents. The pulse shape of the dark current is shown in Fig. 2 for 19 and 29 μs pulses. Measurements of dark current were made using 19 μs pulses.

At low power the dark current pulse was approximately triangular, with a maximum at the end. At high powers we noticed saturation effects produced nonlinearities of the dark current pulse, causing it to turn over. A variety of effects which could contribute to saturation are described below.

Measurements of range of the dark current electrons (described below) indicate that the signal measured with a current transformer contains a significant component of Compton electrons produced from x rays. This Compton signal could consist of perhaps 5%– 10% of the direct measured dark current. This signal may be more forward peaked than the multiple scattered low energy electrons, which penetrate farther in materials.

The dark current measurements are shown in Fig. 3. Measurements at the lowest current levels were made by counting the rate of electrons detected in a 5 cm diameter × 2.5 cm scintillator 15 cm from the window of the cavity. Individual pulses within a 2 μs time were recorded and this electron signal was converted to an instantaneous current. The first time this was tried, we found that the signal $I(E_{\rm acc})$ was nonlinear, with a clear, narrow peak at 4.9 MV/m accelerating gradient. The next day when we repeated these measurements, the peak was not

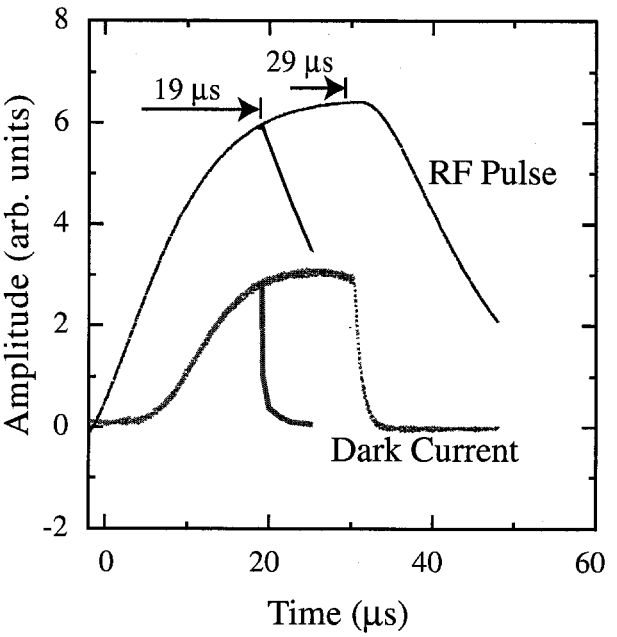

FIG. 2. (Color) Pulse shapes for long and short rf pulses.

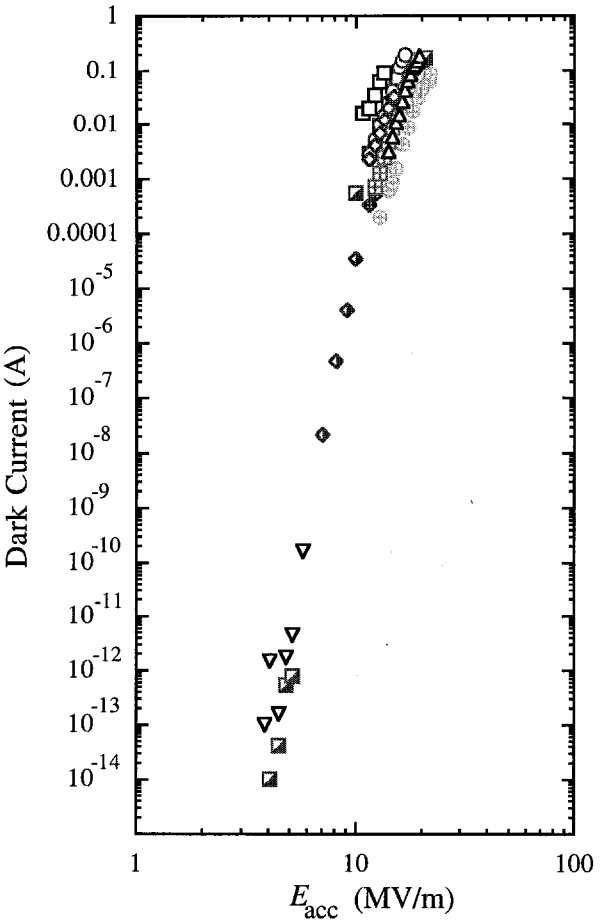

FIG. 3. (Color) Dark current measurements. Data points are identified in Fig. 5, except for low current points taken on August 24 and 28.

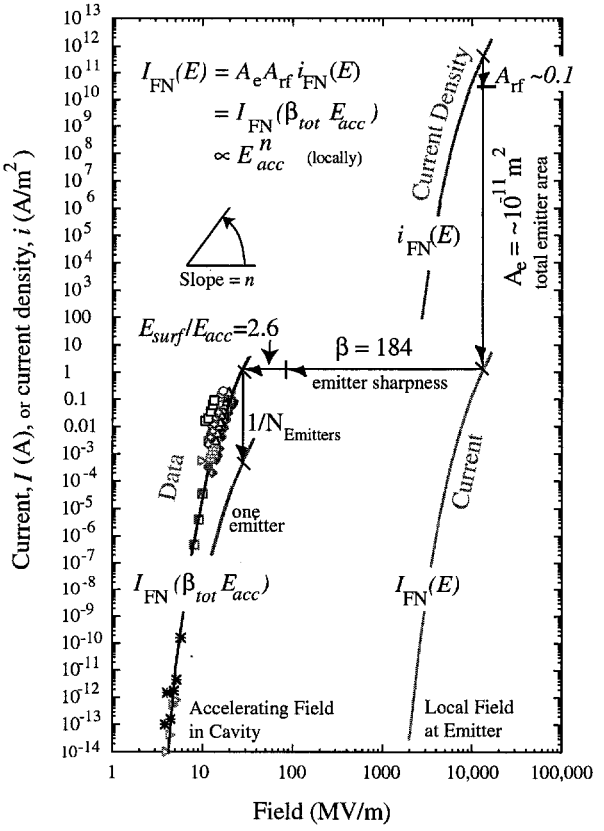

FIG. 4. (Color) The Fowler-Nordheim current density and the factors that determine the measured current, such as the correction for alternating fields, A_{rf}, the emitter area, A_e, the field enhancements, and the number of individual emitters.

there and a simple power law dependence was observed. We assume the temporary peak was associated with multipacting [1] which was reduced by better conditioning. Over a limited range, $I \propto E^n$, with $9 \leq n \leq 30$.

The data at intermediate voltages were taken with a SmartIon radiation meter[26]. This device was useful over about 4 orders of magnitude, but we were able to improve the dynamic range by collimating the dark current beam and renormalizing, where the data overlapped.

Figure 4 shows the overall picture of field emission, with magnitudes of the Fowler-Nordheim current density, the emitter area, A_e, the rf correction factor, A_{rf}, the surface field correction, $E_{surf}/E_{acc} = 2.6$ (for this cavity), the surface field enhancement, β, and the number of emitters, as measured from the pattern of emitted electrons with the field on, described in Sec. III B. An individual emitter seems to have dimensions around 10^{-14} m^2, which can be obtained from the total emitter area of 10^{-11} m^2, assuming 1000 emitters. The number of emitters was estimated from measurements of their density, made with data presented below (as in Fig. 17). We assume that the majority of the current from emitters is detected and the fraction that hits the walls is not a significant perturbation on our comparatively imprecise measurements. With $\beta_{tot} = E_{surf}\beta/E_{acc}$, we measure $\beta = 184$.

1. Initial conditioning

The effect of conditioning can be seen by more closely examining the high current data, as shown in Fig. 5. There was a general trend of the $I(E_{acc})$ data set to move to higher values of E_{acc} over the first two months. The data were fitted to the Fowler-Nordheim expression yielding β_{tot} and A_e. The fitted values of β_{tot} are shown in Fig. 6. The conditioning process was not smooth, and on some days the measured values of β_{tot} were higher and the conditioning was worse. During conditioning at the highest fields, the exponent n was close to 9–10 for weeks. Experimental errors in measuring n are primarily due to nonlinearities of the detectors with small and large signals.

2. Measurements of dark current spectra

The dark current spectrum determines the x-ray background produced. There are two important parameters:

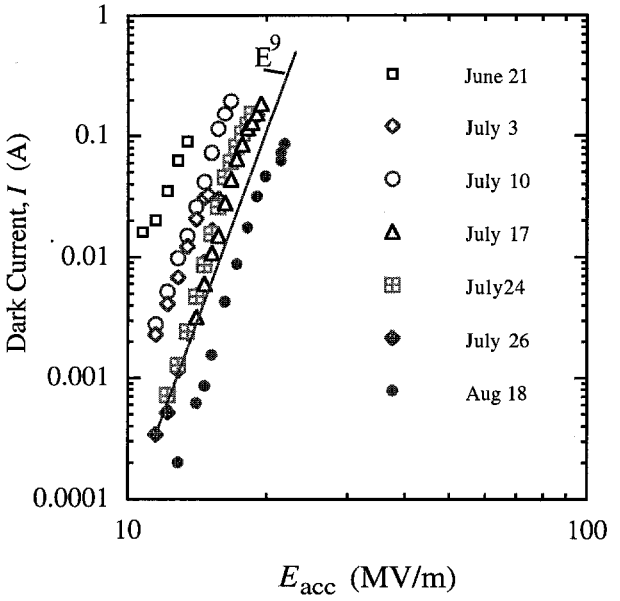

FIG. 5. (Color) High current data during cavity conditioning.

the overall shape of the electron spectrum and the maximum energy of the electrons. We used two methods to measure these quantities. The overall spectrum was measured using range, and the maximum energy was measured with a magnetic spectrometer.

The magnetic spectrometer (Fig. 7) was constructed using thin steel sheets and 2.54 cm thick ceramic permanent magnet material. The gap was 2.54 cm high and 5.08 cm long, and the maximum field of 0.117 T was measured along with fringe field corrections [27]. Since the magnet was so small, an undeviated beam from the slit passed around the magnet and hit the Polaroid film, which permitted an accurate calibration.

The spectrometer is primarily sensitive to the top end of the spectrum because (i) the lowest momenta are bent too strongly to make it through the magnet, (ii) multiple scattering at lower momenta produces a large divergence which penetrates the slit inefficiently, and (iii) lower momenta come from irises close to the slit and these electrons exit the window far from the cavity axis. The spectrum, shown in Fig. 8, indicates that the maximum energy of the electrons is $\sim 0.4\ E_{\mathrm{acc}}L$, where L is the length of the cavity. This roughly agrees with MAFIA calculations of electrons in the cavity, which were designed for muon moving at $v/c = 0.87$.

The spectra of electrons were also measured using range information in plastic, graphite, and aluminum. The beam transformer was placed behind a stack of material and the current which penetrated the material was plotted. This technique is described in Bethe [28]. The spectrum of electrons measured is shown in Fig. 9. We also plot the end point energy expected from 0.4 times the gradient times the cavity length. Multiple scattering of very low energy electrons reduces the range from that expected for linear tracks. There is a large background, presumably due to Compton x rays that penetrates the material and produces electron currents.

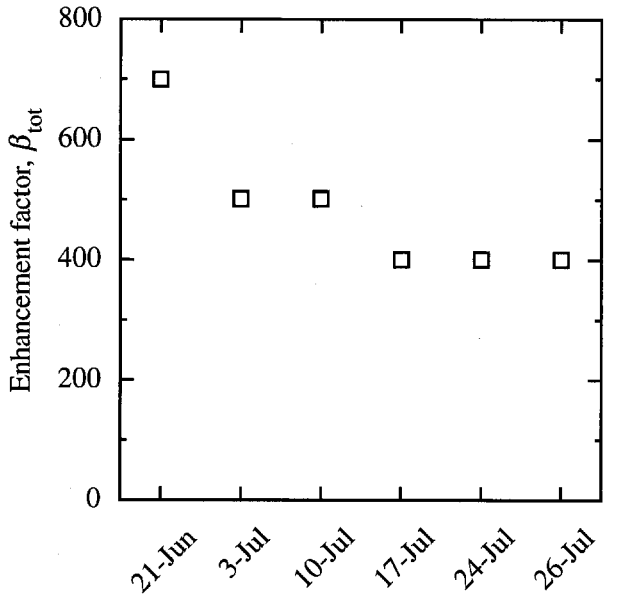

FIG. 6. Progress in conditioning.

3. *Microstructure*

If emission follows a E^9 or E^{10} law, the time structure of the emitted beam from an 805 MHz single cell cavity would be roughly Gaussian with $\sigma = 62$ ps. Since our multicell cavity is tuned for muons with a β of 0.87, and has an active length of 1 m, this narrow width could be spread by $\Delta t = (1 - \beta)L/c \sim 0.5$ ns, where L is the length of the cavity and c is the speed of light. Since the detection efficiency of low energy electrons is reduced due to absorption and multiple scattering, we would expect that any measured spectrum would be narrower than this.

In order to determine the microstructure of the beam, we used a coaxial Faraday cup (shown in Fig. 10), which had been carefully tuned to 50 Ω with a time domain reflectometer with a length of low loss cable to transmit the dark current pulse to a HP 8593A Spectrum Analyzer [29]. The spectrum appeared as a series of harmonics of the 805 MHz driving frequency as shown in Fig. 11, extending to 10 GHz. At these frequencies cable attenuation and dispersion in the approximately 20 m of cable are significant. We corrected the frequency spectra for attenuation but did not have sufficiently precise data to correct for dispersion in the cable to produce corrected time domain plots or accurate reconstruction from phases. We can, however, make the weaker statement that our data are consistent with the predicted frequency dependence.

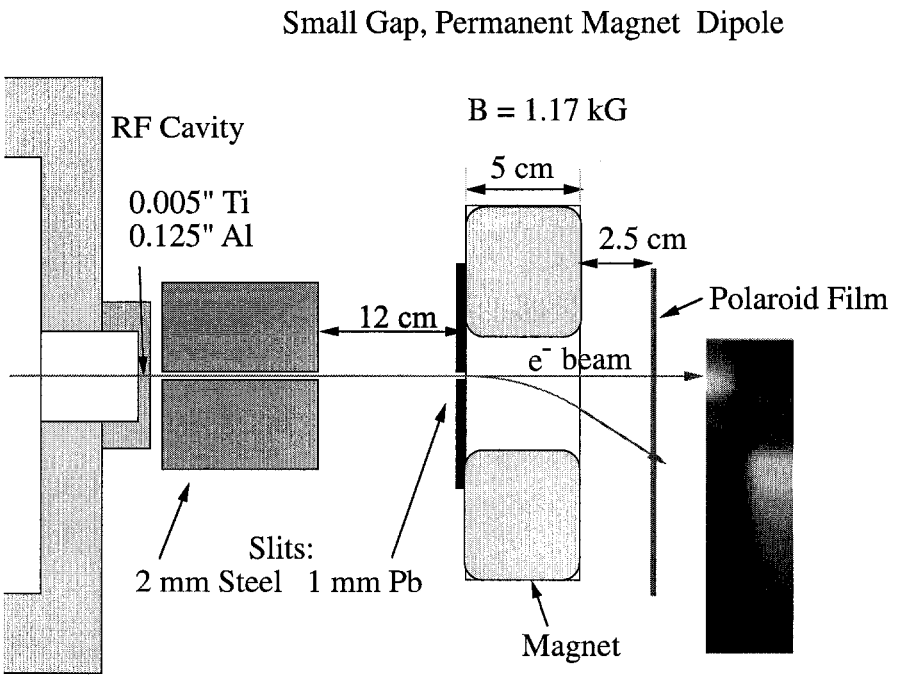

FIG. 7. (Color) The magnetic spectrometer used for dark current energy measurements.

These data were used to reconstruct the shape of the pulse, assuming equal phases of the different harmonics. The result, shown in Fig. 12, is a basically rectangular pulse with a flat bottom. The FWHM of the pulse is about 200 ps, and the flat bottom is about 400 ps long. The duty cycle of the emitted beams, essentially the integral of the curve in Fig. 12 is A_{rf}, the factor used to convert rf field emission to dc field emission. This is done in Sec. V.

4. Vacuum

The vacuum pressure of the cavity varied over several orders of magnitude during rf processing. The vacuum pressure started at 3×10^{-6} Torr when the cavity was first turned on at 70 kW of input power, and stabilized around 2×10^{-8} Torr after 8 weeks of processing at 12 MW. When the cavity was idle (without rf input), the vacuum pressure stabilized around 5×10^{-9} Torr.

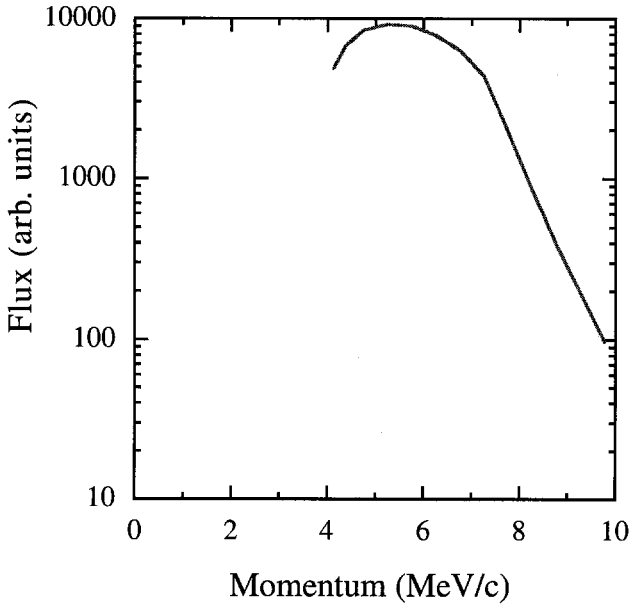

FIG. 8. (Color) Momentum spectrum from the spectrometer for $E_{acc} = 14.1$ MV/m.

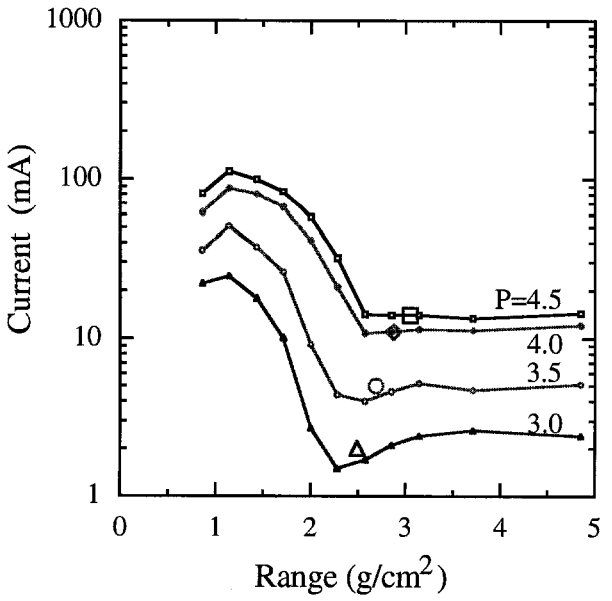

FIG. 9. (Color) Range measurements for different power levels (in MW). The range of the electrons is shown by the symbol.

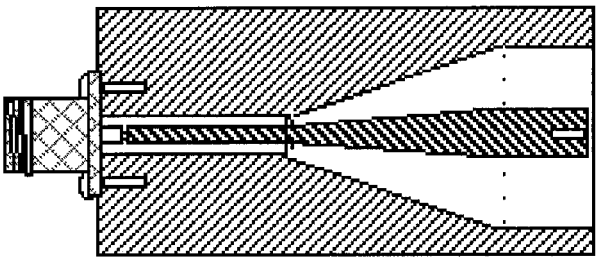

FIG. 10. The Faraday cup; the outside diameter is 5 cm.

During rf processing without the solenoidal field, the vacuum pressure always increased when the input power was raised. Then, after time, it stabilized to a lower pressure as a result of rf processing. The presence of the solenoidal field increased the vacuum pressure to the level of 10^{-7} Torr, an indication of enhanced outgassing. Subsequent rf processing brought the pressure back to a 5×10^{-9} Torr level. The solenoid turn-on required re-processing of the cavity as if it had never been processed before.

The vacuum pressure was monitored using a number of gauges and a residual gas analyzer (RGA), all located in the pumping port at the top of the waveguide coupler shown in Fig. 1. The partial pressures of the gasses seen are shown in Table I and Fig. 13. The base pressure measured was approximately 5×10^{-9} Torr when not pulsing. Breakdown caused the ratio of Cu/gas pressures to increase substantially, and the ratio may be even higher since copper atoms would tend to stick to the walls better than gas atoms, and the RGA time constant is long.

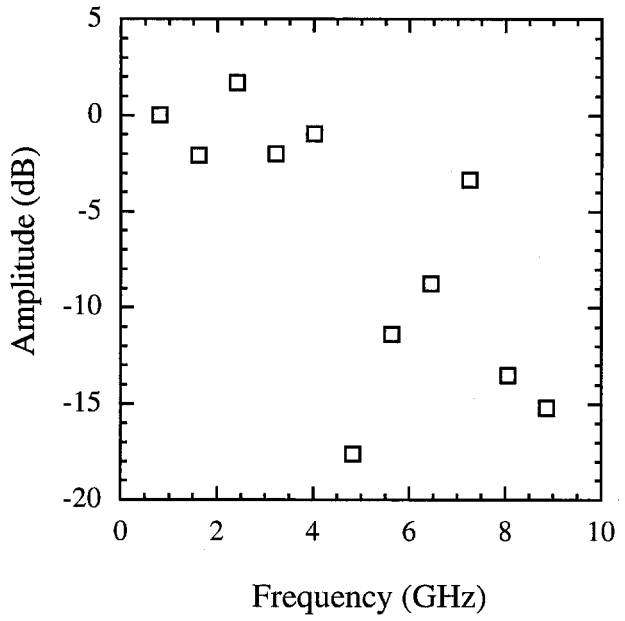

FIG. 11. The frequency spectrum measured with the spectrum analyzer.

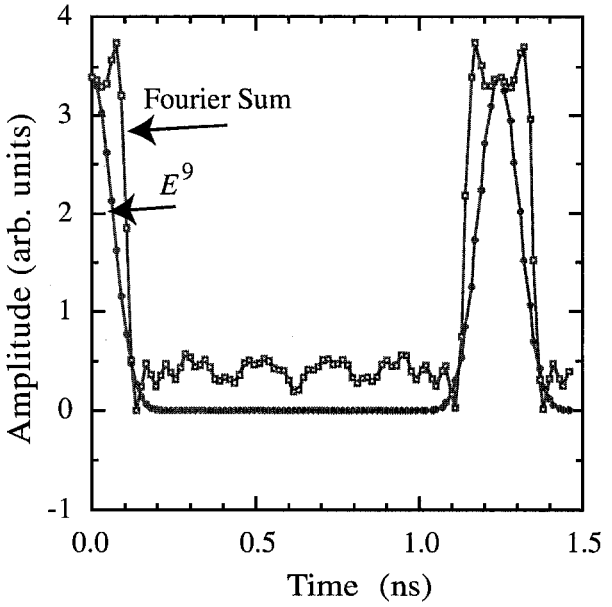

FIG. 12. (Color) The derived pulse shape from the frequency spectrum measurements.

TABLE I. Partial pressures, in nTorr.

Mass	Gas	rf on	rf off	Breakdown
2	H_2	9.2	1.6	
16	O_2	2.5	0.4	
18	H_2O	2.4	0.4	
28	N_2/CO	6	1.8	
44	CO_2	7.8	1.4	
63	Cu	0.1	$\ll 0.1$	0.95

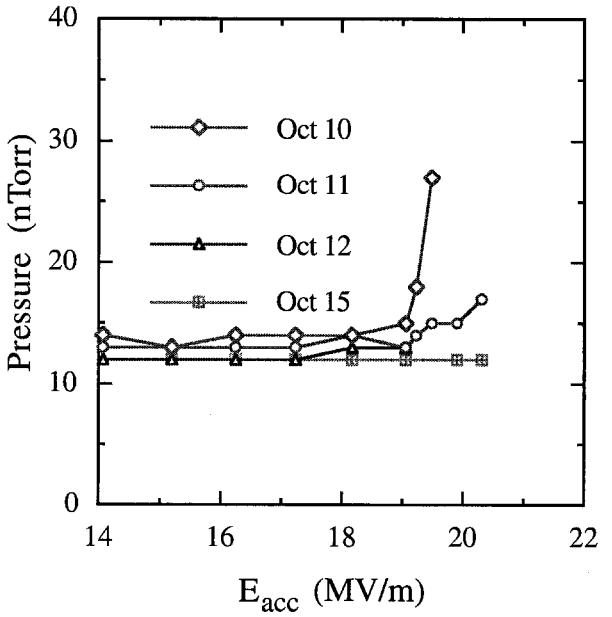

FIG. 13. (Color) Pressure as a function of accelerating field.

The surface conditions of the cavity are, to some extent, determined by its construction. This cavity was machined using a water soluble lubricant, Semcool or Holut 763, followed by cleaning with a microdegreaser, di-water rinse, alcohol rinse, Citronox rub, and warm Citronox bath for 30 min, followed by another di-water rinse and alcohol rinse, after which the components were bagged in nitrogen and brazed. After brazing, all further testing and assembly was done with a nitrogen purge.

5. Nitrogen treatment

There is a large class of discharge cleaning mechanisms which use gas in a metallic chamber. These methods presumably scrub the walls with ions which are produced with the discharge and improve the wall surface. We used nitrogen at a pressure of 10^{-5} Torr to accelerate the conditioning process. The results were obtained at the end of the run after the chamber was damaged during six months of operation, but the conditioning rate obtained was impressive, reducing the dark currents by about 2 orders of magnitude and increasing the accelerating voltage by a factor of about 1.25. This is shown in Fig. 14.

B. B_{sol} = 1–3 T

The initial effect of the solenoidal magnetic field was an increase in dark currents, which required a new program of conditioning. The operation of the cavity was similar to the previous conditioning period before the magnetic field was applied. Following a conditioning process with the field on, however, the cavity operated at comparable electric field levels to those obtained with the B field off, but 4 times higher radiation levels were measured on axis outside the shielding. An accurate measurement of the magnetic field dependence of dark current emission after conditioning, which is one of the goals of this effort, was found to be very difficult. The fields interact with all aspects of the measurement, through the orbits of the electrons, both in and outside of the cavity, the instrumentation used, and the operation of the cavity itself.

The orbits inside the cavity, multiple scattering produced by the windows, and the orbits of electrons as they leave the immediate region of the cavity can be different depending on the magnetic field, and most detectors are sensitive to the geometrical details of the radiation flux. An additional complication is the fact that many detectors do not operate in high magnetic fields. The rf magnetoresistance of the copper was initially thought to be a significant effect; however more careful measurements of cavity losses as a function of the magnetic field in another cavity have shown the effect to be less than $\sim 5 \times 10^{-3}$ at 2.5 T.

A number of methods were studied. We looked primarily at measurements of the radiation levels in the cave using radiation monitors which could see backscatter from the electrons and photons but not the cavity/magnet system itself and we also looked at radiation monitors outside the cave on the magnetic field axis. Radiation levels off axis inside the cave, as shown in Fig. 15, showed less dependence of dark currents on the magnetic field than measurements made on axis outside the cave.

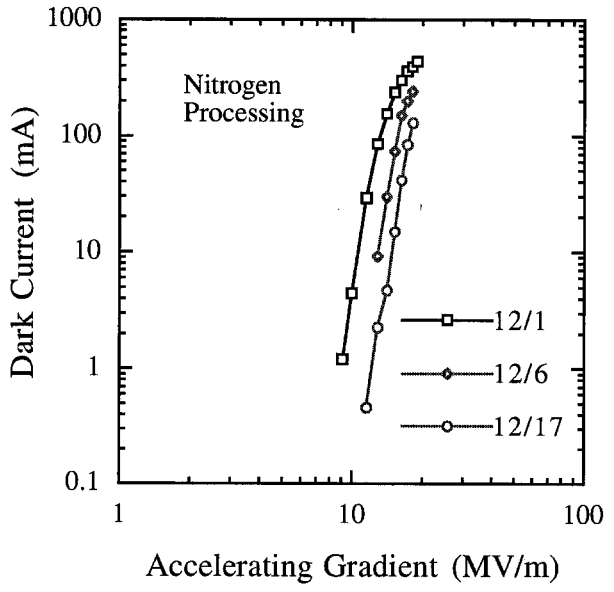

FIG. 14. (Color) Dark current measurements during nitrogen conditioning.

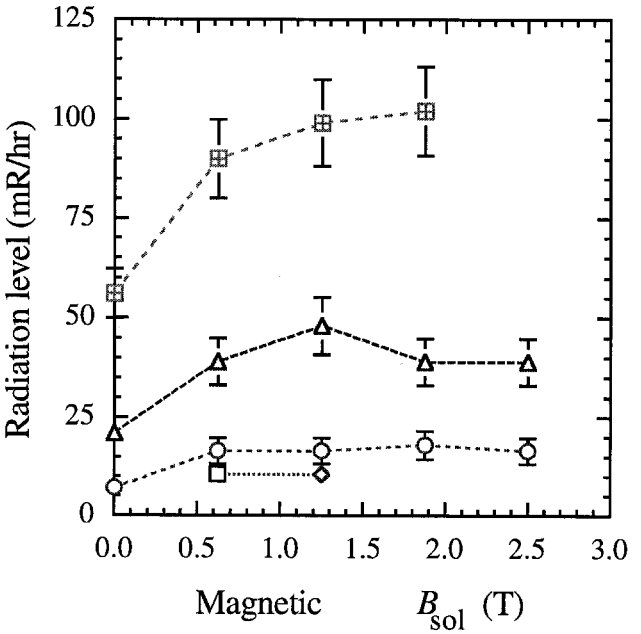

FIG. 15. (Color) Dependence of the radiation levels on the solenoidal magnetic field.

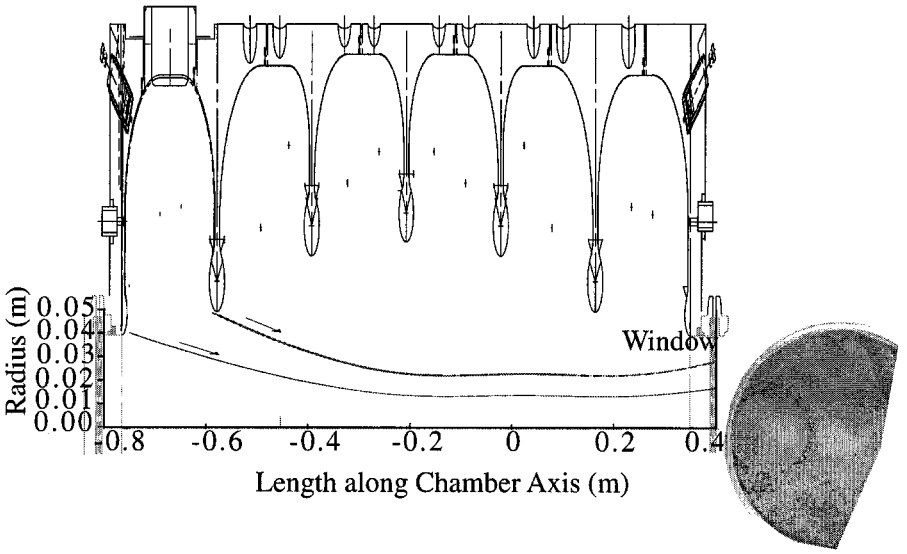

FIG. 16. (Color) The cavity geometry.

Ring beamlets

There were two vacuum failures of the window during the conditioning of the cavity with the magnetic field. When the protective cover of the window was removed, a pattern of burned spots was noted on the outside of the window, forming parts of three concentric bands. These bands seemed to be composed of a number of beamlets. Calculations of the magnetic field from the solenoid permitted the bands to be associated with the irises of the cavity, as shown in Fig. 16. We assumed that the electrons would follow the field lines to the window.

Space charge effects should determine the ultimate size of the beamlets, and these effects have a characteristic dependence on B and E [30]. We then tried to measure the beamlet sizes. When glass plates were placed against the external face of the window, they showed browning from radiation damage due to the electron beam, as shown in Fig. 17. The best spatial resolution of these plates was limited by the multiple scattering in the window and was on the order of 100 μm. Since the electron energy was low, multiple scattering angles were very large. In order to keep the glass close to the concave window it was necessary to use small pieces that could see only part of the band structure. To investigate space charge effects, we varied the electric and magnetic fields. Lowering the magnetic field to alter space charge effects, however, turned the beamlets into rings.

The ring radius was found to be proportional to E and $1/B^2$ as shown in Figs. 18 and 19. The dynamics of these rings can be explained by $\mathbf{E} \times \mathbf{B}$ drifts during the acceleration process. As the electrons accelerate through the mostly axial magnetic field, the radial components of the electric field near the irises produce azimuthal $\mathbf{E} \times \mathbf{B}$ drifts with increasingly large radii. Since the transverse electric field components are not turned off adiabatically, the transverse momentum remains with the electrons as they are accelerated. The radii produced are roughly equal to

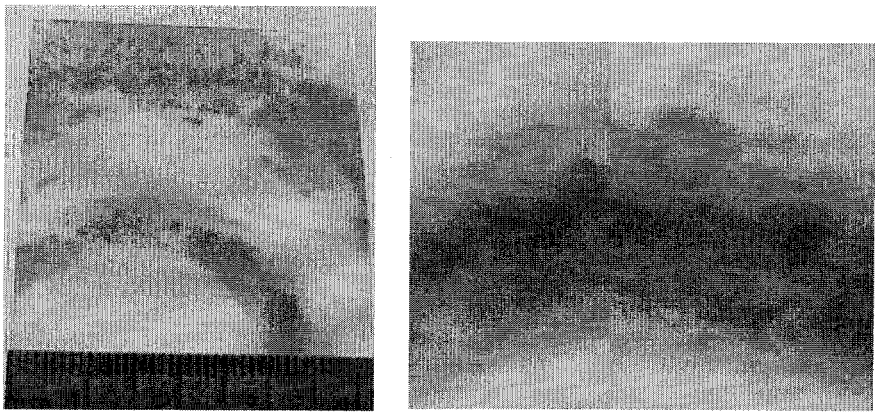

FIG. 17. (Color) The bands and beamlets in them.

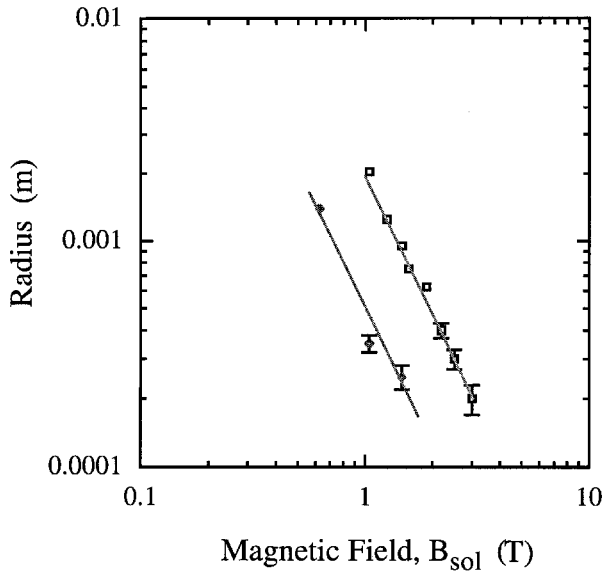

FIG. 18. (Color) Radii of beamlets as a function of solenoidal field. The upper set of data comes from the inner band.

$$r = \frac{\gamma m_0 E_\perp}{eB^2},$$

where $E_\perp$, γ, m_0, and e are the components of the electric field perpendicular to the magnetic field, relativistic gamma, electron rest mass, and charge. This process is commonly seen in foilless diodes and is described in Ref. [31].

All emitters seen in the cavity seemed to produce ring beams; however the diameters of the rings are dependent on the local values of E and B at the point of production. The Helmholtz coil geometry used here produced a rapidly decreasing field at the irises farthest from the coils. Since the diameters of the rings produced from the two different irises should scale like $1/B^2$, and the farthest two irises have solenoidal fields different by a factor of 2 (Fig. 20), with comparable electric fields we would expect the ring radii to be different by a factor of 4, with the outer iris producing the larger rings. This is, in fact, what is seen, as shown in Fig. 18.

The local current density on the wall may determine the local power density produced when beamlets from one face of a cavity strike the opposite wall. We were unable to measure any structure on the window with a width of less than 100 μm.

C. Cavity history

The initial conditioning of the cavity was performed with no magnetic field. Following the successful operation of the cavity with no field, the superconducting coils were turned on in the gradient mode at a field of 3.5 T. After a quench at this field, the magnet was operated in solenoidal mode. A window failure, due to the beams of low energy electrons, then caused a vacuum leak after about a month of running with this field. A second period of operation with magnetic field, during which we were able to understand the dynamics of the ring beams, also ended in window failure. The final operational period in December was devoted to nitrogen conditioning and magnet measurements. This is shown in Fig. 21. The monitor data accurately reflected the dark current intensities.

Measurements of the Q and the resonant frequency were made after the cavity was removed from the experiment. The Q was found to have changed from 15 000 to 13 500, the resonant frequency of the π mode was

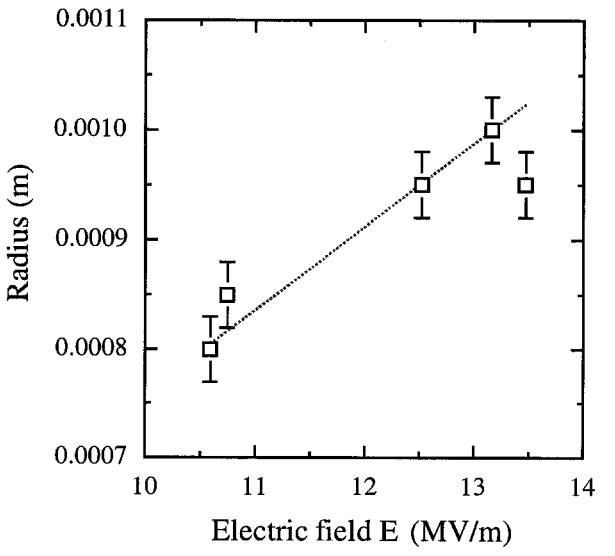

FIG. 19. (Color) Radii of beamlets in the inner band as a function of the accelerating field.

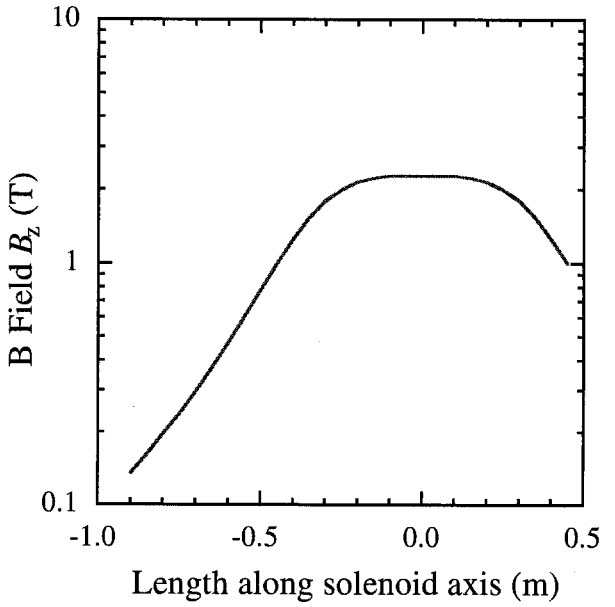

FIG. 20. (Color) The solenoidal field on axis in the cavity.

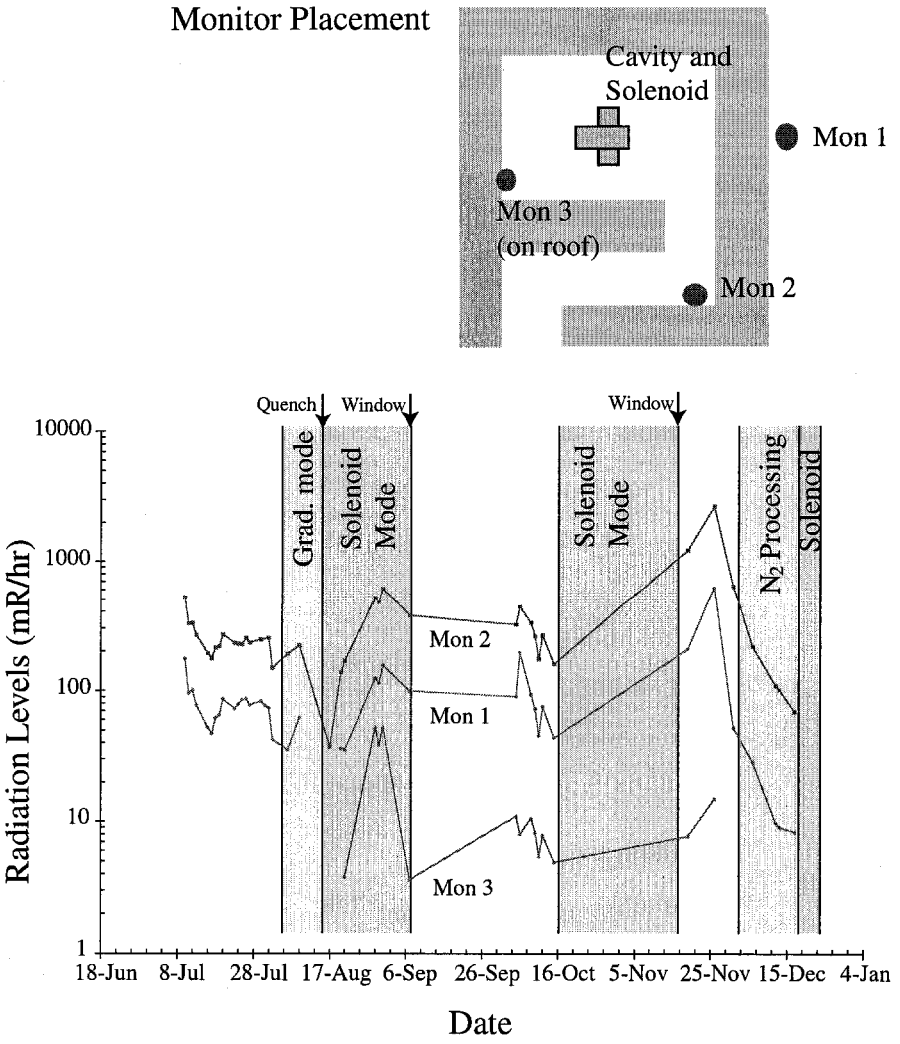

FIG. 21. (Color) The radiation history of the facility during rf processing with and without solenoidal field.

lowered by 13 kHz, and the frequency of the 0 mode was unchanged.

D. Window and iris damage

The titanium window was removed following a vacuum failure. When this window was examined two effects were noted: (1) an array of black spots on the outside of the window, and (2) copper deposition on the inside surface. In fact, the array of black spots seen on the outside of the window could also be seen on the inside, however they were partially obscured by the deposited copper.

The black dots seem to be due to field emitted electron beamlets, which heated the titanium and in a few cases melted it to cause a leak. The distribution of these spots followed the bands described in the previous section.

The black dots on the window could have been produced by local heating due to dark currents. Damage due to breakdown is also a possibility. We can examine the damage produced by the electron beams on the window using the measured beamlet diameter and the approximate magnitude of the dark currents produced by an average emitter. The titanium window will primarily be heated by dE/dx losses and the temperature rise produced will be on the order of $\Delta Q = cm\Delta T$, where c, m, and ΔQ are the specific heat, mass, and absorbed energy of the volume heated by the beam. Both the titanium and copper will undergo heating on the order of 30 K/mA, so localized beamlet currents on the order of 50 mA would be sufficient to melt the window. The time constant for the decay of this heating would be about 10–100 ms, so both long pulses and high beam currents would contribute to window damage. Microscopic examination seems to show that the copper was melted over a larger radius than the titanium, which is consistent with its lower melting point.

The copper deposited on the inside of the window seems to be produced from liquid copper droplets hitting the flat window surface and splashing. An example, somewhat larger and cleaner than most of the droplets,

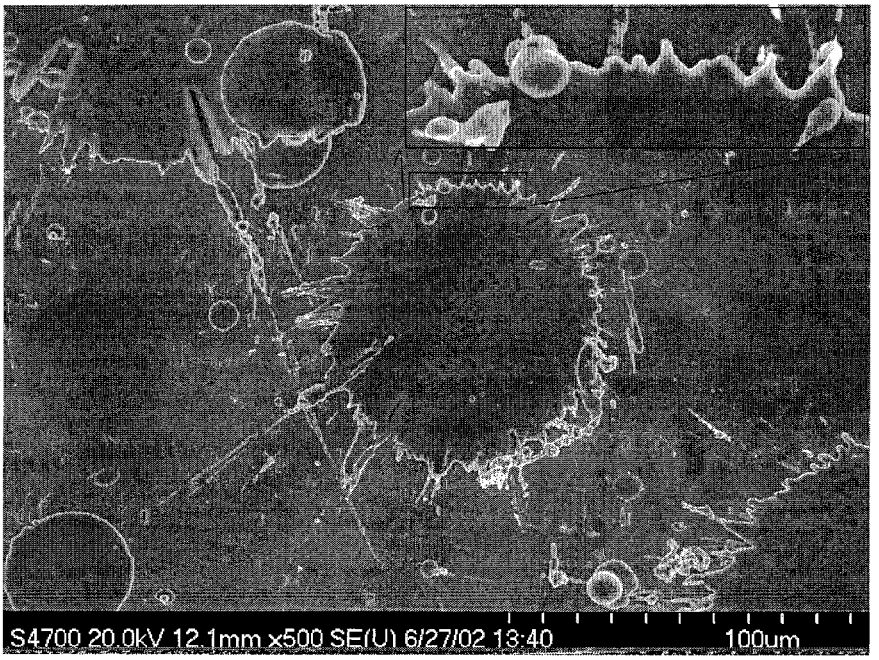

FIG. 22. A scanning electron microscope image of copper splattered on the inside of the window. The area covered is approximately 180 × 250 μm. The inset shows the fine structure of the bumps ringing the splash.

is shown in Fig. 22. The splash seems similar to what one obtains when liquid solder is dropped on the floor. Note that in addition to the large circular splash, there are a number of long hairlike strands visible in the picture. These hairlike strands, and the points that seem to be visible at the edge of the splatters, could produce very efficient field emission sources.

The circumference of the ring shaped splashes is composed of a row of cone shaped bumps about 3–10 μm long with tip radii from 0.1 to 0.5 μm. These bumps are consistent with β values of 6 to 100. The copper "wires" have lengths of up to 100 μm and diameters as small as 0.5 μm, perhaps consistent with $\beta \sim 200$ if they were able to stand on end.

The overall distribution of copper droplets is basically smooth, with no obvious correlation with the electron produced bands described above. There is a slight increase in the density of droplets near the edges of the window, associated with a reduction in the average size, and this might be due to droplets bouncing off the inside of the tubes immediately in front of the window. If the particles were produced with a velocity of about 10 m/s or greater, these droplets could travel ballistically from the irises to the window with very little deflection, which would explain the even distribution of deposited copper over the area of the window.

The copper irises were also damaged during operation. The damage occurred as pitting, uniformly distributed over the surface of the high field part of the irises. The two irises near the center of the cavity were damaged more than the ones on the ends and the irises near the input coupler were damaged less than the ones at the other end. Presumably the damage is a sensitive function of the surface electric field and it is unlikely that this would be precisely equal for all seven irises. Typical damage is shown in Fig. 23.

We have constructed a periscope/microscope which can look in detail at the spark damage on the irises of the cavity and have begun to study the material that has been removed and transported by arcing. An image of the surface of the central iris is shown in Fig. 24. The surface shows shiny spheres of deposited copper sitting on the machined surface and a variety of other features. The size of most of these features is less than 100 μm. Small

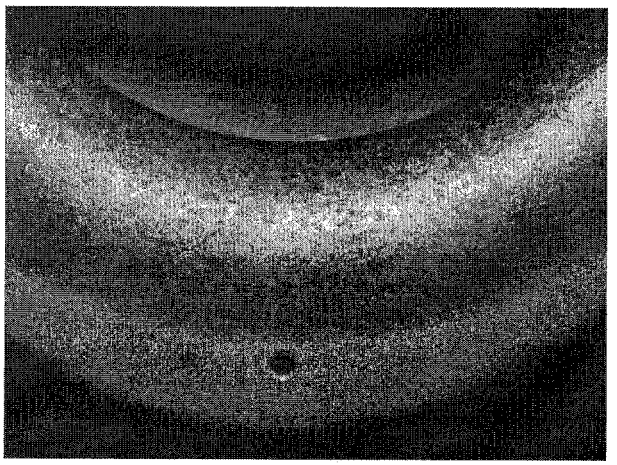

FIG. 23. (Color) Damage on the irises.

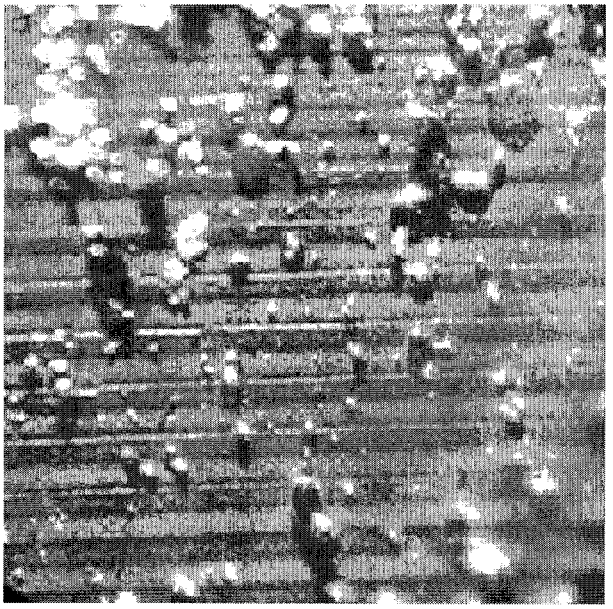

FIG. 24. (Color) A microscopic image of the center iris in the cavity, covering an area about 1000×1000 μm.

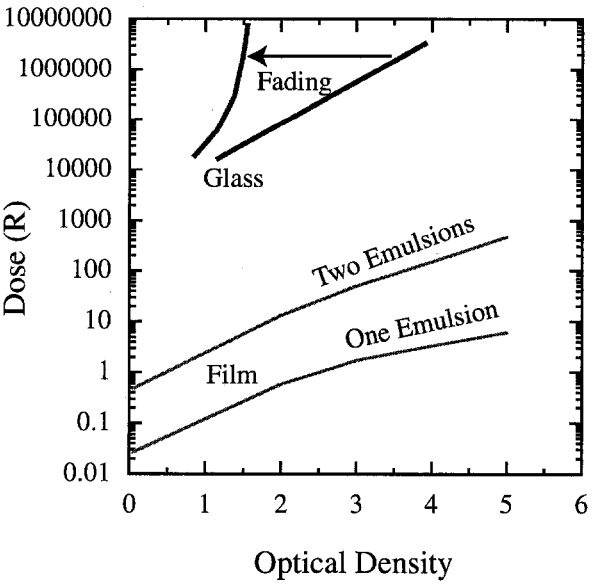

FIG. 25. (Color) Type 2 film parameters with an approximate glass response curve.

spheres deposited on large spheres could produce the enhancement factors described in Sec. II.

E. Instrumentation

This paper describes measurements made on signals which vary over a wide range, in some cases 14 orders of magnitude. A variety of techniques were used, each of which had its own limitations: beam transformers, scintillator/photomultiplier tubes, thermoluminescent detectors, portable radiation monitors, Faraday cups, Polaroid film, personal monitoring film, area radiation monitors, glass plates, residual gas analyzers, range spectrometers, magnetic spectrometers, and a variety of other standard instrumentation [32,33]. Each of these techniques is useful over a comparatively small range of parameters. The most useful methods tend to be those in use as radiation monitors [33]. The type 2 personal monitoring film has two emulsions and is useful over about 4 orders of magnitude in radiation dose, as shown in Fig. 25. Polaroid film is useful over a much narrower range and much less radiation dose. Normal glass can be used at higher doses, but the glass fades somewhat (even in the dark) in as little as 24 hours, so the linearity is no longer useful.

We checked that different techniques for measurements tracked consistently, whenever possible. The linearity of these techniques over many orders of magnitude in signal, with the additional presence of radiation fluxes at high power levels (up to MW levels) and changing pulse shapes, was not continuously verified with high precision.

IV. OTHER RECENT MEASUREMENTS

The Fowler-Nordheim dependence of current on accelerating field seems to be a common feature of many types of accelerating structures. At high fields this appears as a power law dependence of the dark current, radiation level, or energy loss (lowered Q) on the electric field. At lower electric fields, the dependence of the Fowler-Nordheim equation effectively increases the power law to E^{15}-E^{35}. At higher fields the dependence looks like $E^{9.6}$. This behavior seems to be characteristic of a wide range of accelerating structures. It has been shown that x-ray fluxes external to accelerating cavities with low energy electrons are primarily composed of 100 keV x rays, which are roughly isotropic [11]. The lower energy of these x rays is determined by the photoelectric effect, and their angular distribution is determined by electron multiple scattering and the Compton effect.

Both CERN superconducting rf cavities and an ANL photoinjector constructed at the Taiwan light source give radiation levels measured nearby that are proportional to $E^{9.6}$ [11,34]. These data are consistent with the results presented here.

Superconducting rf cavities also seem to show the same effects. The quality of superconducting cavities is described by a plot of the operating Q, a measure of the stored energy divided by loss per cycle, as a function of accelerating field [1]. Losses in a cavity, however, are more intuitively measured by $1/Q$. We have plotted these curves for three cavities in Fig. 26. The data are consistent with the energy loss being the sum of a constant, due to the residual resistivity ratio, and a rapidly rising loss dependent on E^n, with n in the range 10–20. We assume that this rapidly rising term is entirely due to dark current

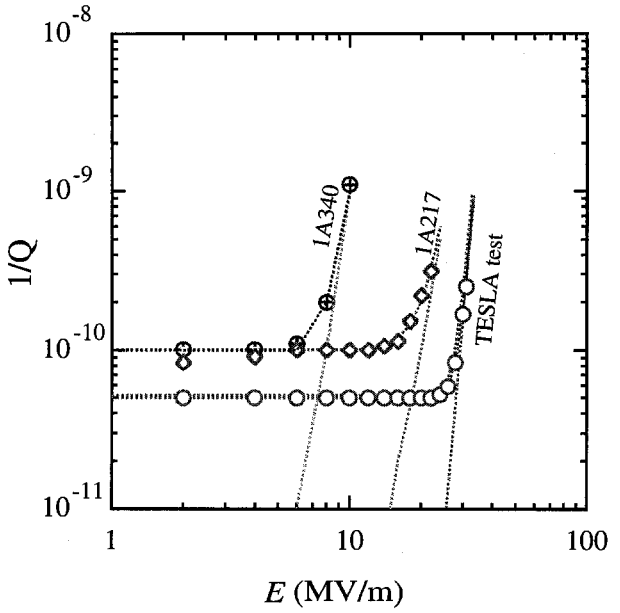

FIG. 26. (Color) SCRF cavity losses from Ref. [1].

losses in the structure and have calculated the required current to generate these losses and the power law dependence on the accelerating field. When currents derived from the $1/Q$ measurements are plotted with the 805 MHz data, both show similar current levels and power law dependence, at least for the worst superconducting structures, as shown in Fig. 27. On the other hand, the best cavities, to be used in the TESLA program, operate with 3 times the electric field and 10 orders of magnitude lower dark currents than our cavity [35]. We have also calculated the local emitter field in a high gradient superconducting cavity using the slope of the steep part of the $1/Q(E)$ curve giving an estimated gradient of ~13 GV/m [36].

The very aggressive research and development effort to produce superconducting cavities which operate at higher fields has been quite successful [1,35]. This increase was obtained primarily by means of careful attention to surface cleanliness and elimination of defects, which implies that comparable gains are possible for copper cavities.

We have also looked at x rays produced at the ISIS [37] and IPNS [38] proton linacs. These 200 MHz drift tube linacs were constructed long ago and are now the basis for pulsed neutron programs. Radiation measurements for both accelerators show that the x-ray dose in the immediate region of the drift tube linacs is proportional to E^{14}, which is consistent with the power law followed in the middle region of the data shown in Fig. 3. Again this seems to imply that Fowler-Nordheim dark currents are the dominant mechanism. ISIS data show an exponent n of 13.5–14, as shown in Fig. 28.

Data from the IPNS linac show an E^{14} dependence of the radiation flux on the acceleration field, Fig. 29, when

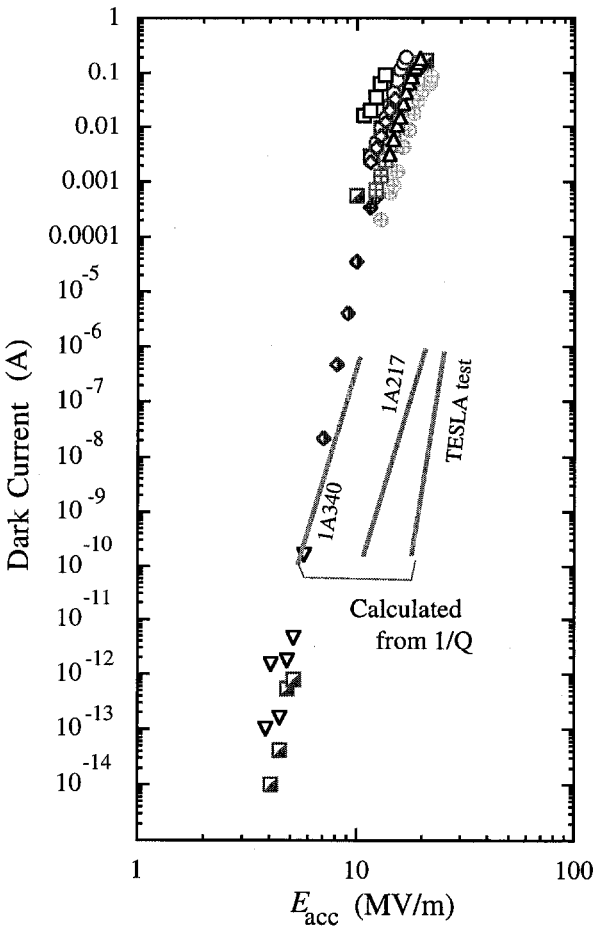

FIG. 27. (Color) SCRF dark currents compared with the 805 MHz cavity.

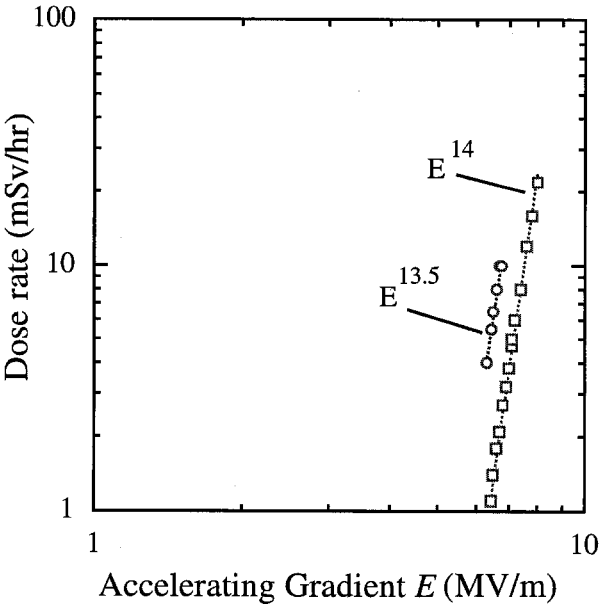

FIG. 28. (Color) Radiation levels near the ISIS linac sections.

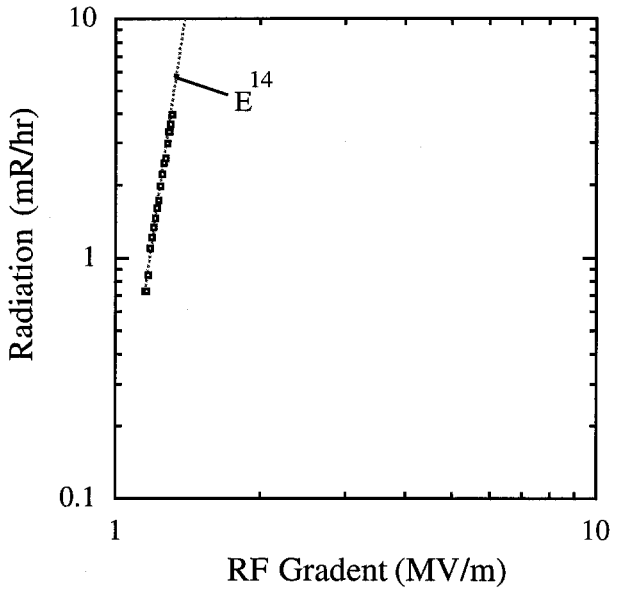

FIG. 29. (Color) Radiation fluxes near the proton linac of IPNS.

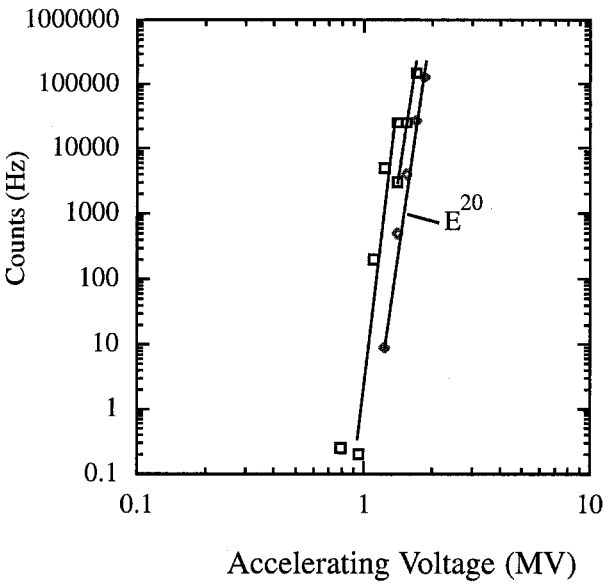

FIG. 31. (Color) X-ray fluxes from an rf cavity operating in the CESR ring.

the radiation flux was measured about halfway down the linac tank.

Measurements of an NLC prototype cavity show an E^{15} dependence on the field as shown in Fig. 30 [39].

Measurements of x-ray fluxes and energies in a superconducting cavity in the CESR storage ring have been made at Cornell to evaluate the feasibility of single particle detectors in the region of the cavities [40]. In this measurement the x-ray detector was placed at some distance from the cavity and did not view the emitting surfaces directly. Nevertheless, as shown by the data in Fig. 31, an E^{20} dependence on accelerating voltage again implies that Fowler-Nordheim field emission is the dominant process. In this experiment, as in the measurement of the Taiwan photoinjector gun, the photon energy was measured, showing a wide spectrum with a geometric mean energy of about 100 keV.

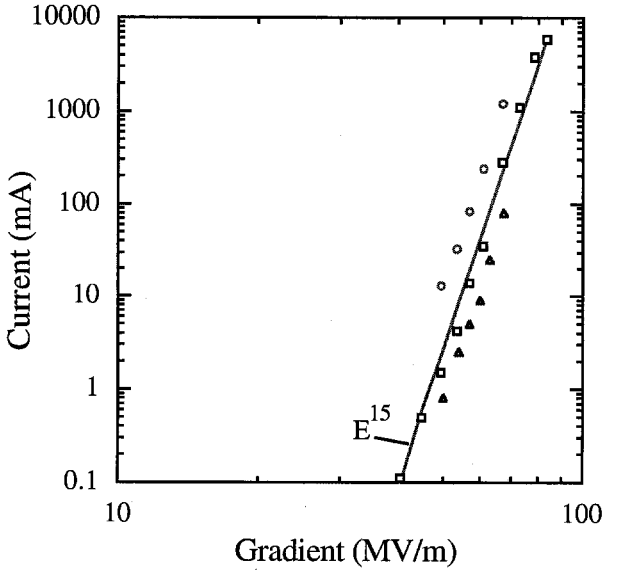

FIG. 30. (Color) Dark currents from an NLC prototype cavity.

We have also examined data on radiation levels and cavity breakdown which was taken during the tune-up of the Fermilab linac upgrade [41]. These data were collected systematically during the operational life of this linac. Data from the conditioning period of the Fermilab 805 MHz linac upgrade show that the sparking rate is strongly correlated with the radiation level measured near the cavities as shown in Fig. 32. These data incorporate both periods of conditioning, when the cavity field levels were being increased, and normal operating conditions, when the cavity fields were fairly stable. The raw sparking rate is seen to be directly proportional to the radiation level, implying that the two effects are related. The causal relation involved here is not well understood.

V. THE PHYSICS OF EMITTERS

We are interested in a number of issues, such as how emitters are activated, how one can deactivate them or minimize their effects, and how dark current emission is related to breakdown. Unfortunately, these data provide only indirect information on the nature of the emitters. We describe how our data are sensitive to a variety of phenomena.

We define the exponent of the emission law as

$$n = \frac{E\,dI}{I\,dE},$$

with I and E as the current and field, respectively. It is possible to derive information about β_{tot}, and other

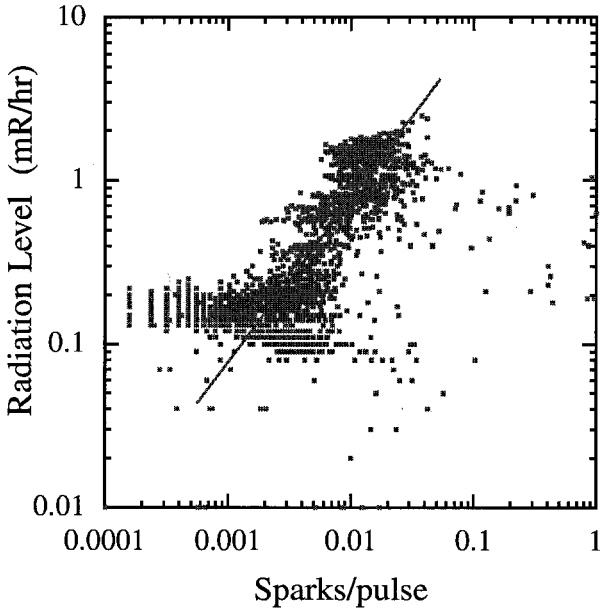

FIG. 32. (Color) Fermilab linac data on the correlation between the sparking rate and the ambient radiation level in the linac enclosure, an indirect measure of dark currents. These data were accumulated over many months.

parameters, directly from knowledge of the exponential dependence of dark currents or x-ray fluxes. This $I \propto E^n$ dependence is shown in Fig. 33. Measurements with current transformers or radiation monitors outside the shielding give values of $n \sim 9.6$ corresponding to high currents. Radiation monitors inside the shielding give values $n \sim 15$ and measurements which count individual photons and are sensitive to small currents give $n \geq 20$. This can be explained by the fact that more sensitive instrumentation sees the $n(E)$ dependence where the exponent is higher, and less sensitive instrumentation sees higher currents produced where the field emission curve becomes flatter.

It is possible to estimate the order of magnitude of the current per emitter from the total current and the density of emitters as determined from the beam profiles, seen in Fig. 17. Using an emitter current of 10 mA, and a density of 10^5 emitters/m^2 obtained from measurements like Fig. 17, one calculates an average current of 10^{-5}, assuming all emitters are roughly comparable.

A. The correction for sinusoidal fields, A_{rf}

The Fowler-Nordheim parametrization assumes that the electric field is constant, whereas it is actually varying sinusoidally with the rf phase ϕ. We have seen that the actual pulse of current appears only for about one-tenth of the rf period. Since the current can be approximated by E^n, the integral can be evaluated numerically and

$$A_{\mathrm{rf}} = \frac{1}{\phi}\int \sin^n \phi d\phi \sim 0.1,$$

when evaluated over many cycles (and only positive polarities); A_{rf} has the dependence shown in Fig. 34. This issue has also been considered in a more detailed way, producing a more complicated expression for the Fowler-Nordheim process [42,43]. For most measurements, $j_{\mathrm{rf}}(E) \sim 0.1 j_{\mathrm{dc}}(E)$, and the $A_{\mathrm{rf}} \propto E^{0.5}$ dependence is a small correction within statistical and systematic errors.

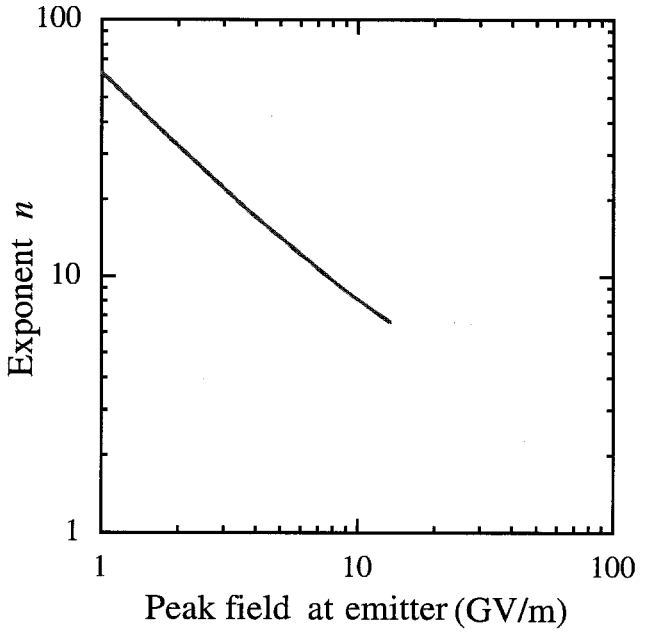

FIG. 33. (Color) Dependence of exponent, n on the peak field at the emitter.

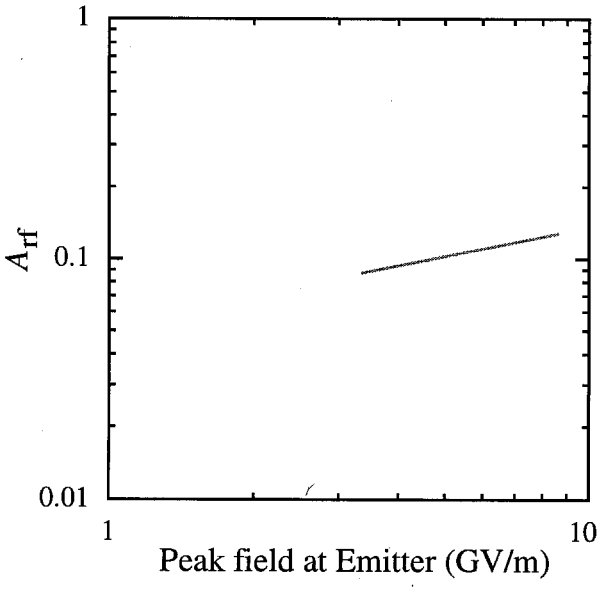

FIG. 34. (Color) Dependence of the rf correction factor, A_{rf}, on the emitter field, from integration.

B. Tensile stress and tensile strength

An active field emitter interacts with very high electric fields, since measurable currents require electric fields at the tip of the emitter of $E = \beta_{tot} E_{acc} \sim 4$–$10$ GV/m. This produces high current densities, local heating, and enormous forces, which act on the tiny tip of an emitter. The mechanical tension induced by the electric field is given by $T = 0.5\epsilon_0 E^2$, which gives tensile stresses in the range of $-(320$–$380)$ MPa ($\sim 40\,000$ lb/in^2). This is equal to the tensile strength of copper [44]. The primary mechanical limit would be when the tips snapped off. We assume that this would result in breakdown of the cavity.

The lowest values of the exponent n seen in our data are ~ 9, comparable to the tensile strength of work hardened copper, and these are compatible with a surface field of 8 GV/m. This is significantly above the ~ 100 MPa (10 000 lb/in^2) stress at which soft annealed copper will begin to deform. More conservatively operated cavities run at values of $n \sim 14$, corresponding to a gradient of 5 GV/m and a tensile stress of ~ 120 MPa, after having been conditioned at higher fields. This is shown in Fig. 35. When installed, most cavities should be soft from annealing, but stresses of this magnitude would locally work harden them, as shown in Fig. 35 and Table II. Conditioning, which seems to operate at surface stresses comparable to the maximum strength of copper, may thus consist of simply tearing off all the sharpest emitting surfaces in breakdown or sparking events.

The mechanical stress exerted by the electric field on the point of an emitter should be also sufficient to bend and move objects so that an emitter tip is perpendicular to the plane of the local surface of the structure, or weld particles to the surface [1]. This could be one mechanism for activating emitters. It is interesting to note that tensile stress and tensile strength arguments apply to normal, superconducting, and dielectric structures.

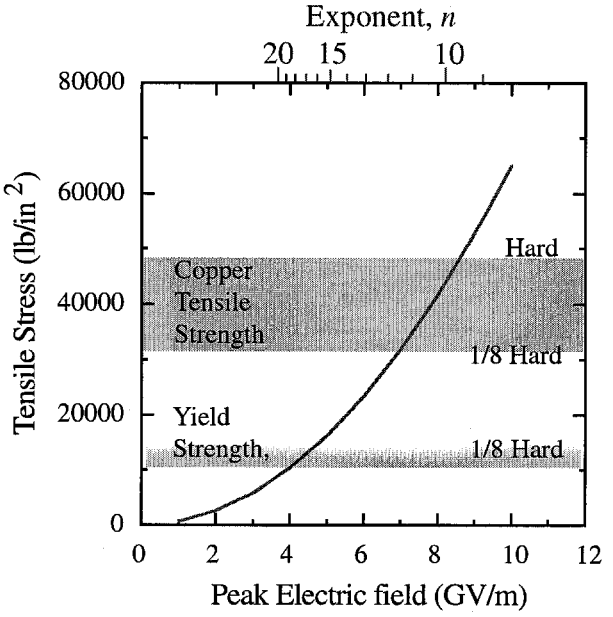

FIG. 35. (Color) Stress at emitters as a function of local field E and the exponent n.

TABLE II. Pressure on emitter surfaces.

Structure	n	E, GV/m	$-P$, MPa
This experiment	9.0–30	2.2–9.4	21–391
ANL/Taiwan	9.6	8.60	327
ISIS	13.5–14.0	5.50–5.75	134–146
IPNS	14.0	5.50	134
NLC prototype	15.0	5.05	113
CESR SCRF	20.0	3.60	57

The surfaces of field emitters have been studied for many years, in part because the field emission pattern shows the geometric structure of the atomic surface. Dyke *et al.* [45] showed that a combination of tensile stress and surface tension could either sharpen or dull emitter tips at rates that depended very strongly on temperature. These processes require high temperatures (~ 1400 K), or long times (hours), or both. This work was expanded by Gufel'd [46] and van Oostrom [47] who mentioned the high stress levels involved and the possibility that solid microparticles could be emitted into an interelectrode gap, although the assumption in these papers seems to be that breakdown is a result of melting of surface projections or local gas pressures above 10^{-3} Torr.

The dependence of the exponent n on the accelerating field is shown in Fig. 36. As conditioning improved, the measured values of n stayed roughly constant, while the accelerating field increased. There is scatter in the points, primarily due to systematic errors in the evaluation of n.

Measurements of breakdown in a variety of geometries show that breakdown occurs at fields of roughly $E \sim 10$ GV/m, and the properties of breakdown events are highly dependent on the nature of the metallic surface, which is consistent with this model [5,48]. While systematic measurements have been made with different materials, these measurements are old and did not include detailed knowledge of the surface or alloy of the material [49,50].

C. Emitter heating and other effects

Although many models have considered melting or gas emission as part of the trigger for breakdown events, the very high stresses we infer at the emitter tips seem incompatible with the presence of molten metal. In order to study the thermal properties of the emitters, we assume that these emitters look like the conical bumps we see in Fig. 22, however some scaling arguments are important.

The thermal response of an emitter is dominated by its size. If a protrusion shaped like a cube of side d sits on a plane, transmitting a current I, with resistivity ρ, the

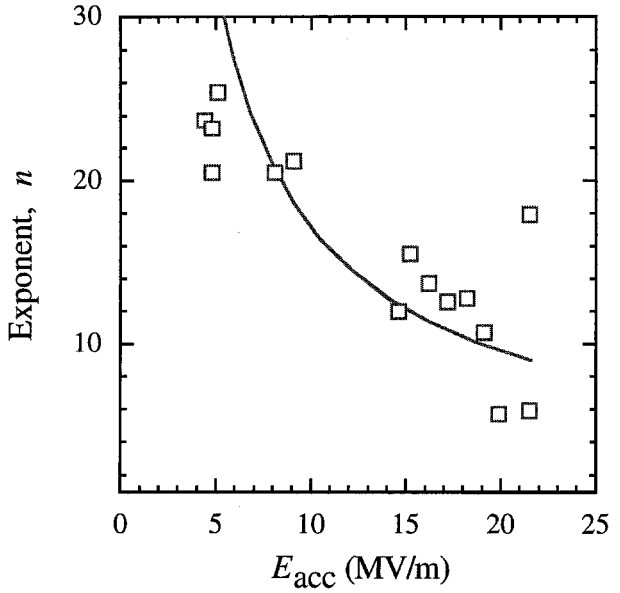

FIG. 36. (Color) Experimental values of $n(E_{acc})$ during conditioning. The smooth curve corresponds to the line in Fig. 33.

resistive power into the cube scales as $P_\Omega = I^2\rho d/d^2 \sim d^{-1}$. The temperature will go as $\Delta T = P_\Omega \delta t/cm \sim d^{-4}$, in time δt where c is the specific heat and m is the mass of the element (with $m \sim d^3$). The thermal power lost by conduction is $P_{cond} = k\Delta T d^2/d \sim d$, where k is the thermal conductivity. The time constant for the heat to be conducted away is $\delta t = cm\Delta T d/kd^2\Delta T \sim d^2$, assuming a temperature difference, ΔT, across the element of length. Thus small emitters get hotter than large ones, although they cool off faster.

Numerical estimates of heating, assuming a copper resistivity, ρ, of 1.7 $\mu\Omega$ cm, specific heat c, of 0.092 cal/g/°C, for conical emitters with an opening angle of 1 sr, and no thermal losses, give a maximum temperature rise of $\Delta T_{tip} \sim 7I^2 r^{-4}\delta t$, where the I is the current in mA, r is the radius in 0.1 μm, δt is the pulse length in μs, and ΔT_{tip} is in °C. From Figs. 4 and 22, we can evaluate the size of the current and area associated with each emitter. We see currents of $<1 \times 10^{-4}$ A, the emitter dimensions are on the order of 0.1 μm, and pulse lengths are on the order of 10–30 μs. In this parameter range we expect the temperature of the emitter tip to increase by only a few degrees. The time scale for heat loss due to conduction is 4 to 6 orders of magnitude shorter than the rf pulse length. Thus, conduction losses would significantly limit the temperature of the emitter tips with emitters of this geometry.

For a copper emitter with an essentially conical geometry, equating the Ohmic power and thermal loss, and solving for the temperature difference gives $\Delta T = I^2\rho dz_e^2/kA_e^2$, where dz_e is the element length and A_e is the area, so the temperature depends on the geometry as dz_e^2/A_e^2, which implies that long thin emitters would get much hotter than short wide ones.

On the other hand, geometry affects both electrical and thermal properties, and emitters which may not be thermally coupled to the body of the cavity have been seen [1]. These complex geometries are more difficult to model, but would be expected to become much hotter than structures thermally coupled to the surface.

Other effects which could contribute to the emitter environment are chemical and structural changes in the material itself [19,51]. Copper normally forms an oxide with very poor electrical conductivity. It has been shown, however, that in the presence of high electric fields the surface can produce conducting filaments through the copper oxide effectively making a permanent breakdown channel [51].

The dominant limitation on the emission of current from a surface is the Child-Langmuir limit, which gives the maximum current density, in A/m^2, as

$$i = 2.33 \times 10^{-6} V^{3/2}/d,$$

where V and d are the voltage and plate separation in a parallel plate geometry [30,31]. In the case of a point emitter, this effect results in a $I \sim E^{3/2}$ dependence of the dark current. We see such an effect in Fig. 14, but only at the highest current, where it is impossible to discriminate between space charge effects and current saturation due to dark current driven energy loss in the cavity.

D. Possible mechanisms for emitter formation

The splashes of copper seen on the windows should produce field emission and breakdown initiation sites. The submicron sized points seen in Fig. 22 are consistent with the dark current intensities and the density of sites implied by Fig. 15, however, other sources of emission are possible. There is also a question of the source of the first breakdown sites, before material was splashed on the walls, and the nature of mechanisms which seem to be able to turn sites on and off.

Nonmetallic emission sites are possible. Data from KEK show densities of ~100 particles/cm^2 deposited on test silicon wafers; most of these particles had dimensions less than 1 μm [1]. We presume that the majority of this material is dielectric, primarily aluminum and silicon oxides, the primary constituents of the Earth's crust. It has been shown that large quantities of finely ground rock can be in the atmosphere. Wyoming, for example, has lost ~200 000 km^3 of material by erosion over ~2×10^7 yr, a significant fraction of it by wind erosion [52]. Measurements at Saclay show that Al_2O_3 and SiO_2 particles on gold or niobium surfaces did not emit in dc fields but became strong field emitters in high gradient rf fields following dielectric heating, which changed their resistivity. These particles can be heated to the point where they glow brightly [53]. Dielectrics, heated to a temperature where they become partially conductive, could be

subject to the same electrostatic forces as metallic emitters, and could cause breakdown.

Once field emission has begun, breakdown at field emission sites will deposit much of the stored energy of the cavity locally in the copper, making and ejecting liquid droplets which splash and make more and perhaps better, emitter sites. Each splash could produce emitters in the sharp points around the circumference and the "wires" shown in Fig. 22 would make excellent emitters if they were bent perpendicular to the surface by electrostatic forces. The simplest model of enhancement factors, as hairs with an aspect ratio approximately equal to β, could thus be produced naturally [2].

E. A "cold copper" breakdown model

Breakdown has been studied and described by Kilpatrick [54]. Plasma effects, driven by ionization of adsorbed gas, are currently believed to be the dominant processes involved in breakdown [8]. The high stresses due to electric fields may also be an important component in breakdown events. While adsorbed gasses are frequently assumed to be involved in breakdown, one can consider options which do not involve gasses.

If emitter tips were resistively heated, it is possible that the tensile stress on the sharpest point could pull the metallic surface out, effectively extruding a "hair" out of the wall of the material. This process would be limited by work hardening of the cooler copper material at the base of the hair, but a hot pointed surface may represent an unstable equilibrium, where the surface will tend to become hotter and sharper as resistive heating and tensile stresses evolve. We have shown in Sec. V B that tensile stresses can be very large, and in Sec. V C that emitter temperatures may be low.

The data on dark currents during conditioning presented in Sec. III imply stresses near the tensile strength of the copper structure during conditioning. A straightforward assumption is that these emitter tips simply fracture and the copper fragments are propelled into the cavity. While bulk heating of metal may occur, it is not essential to the generation of a breakdown event. If a fracture occurs, the fracture line, on both fragment and structure, will produce sharp angles on an atomic scale. Since, as pointed out by Feynman *et al.* [55], the local field enhancements on metallic surfaces are proportional to $1/r$, where r is the local surface bending radius, these sharp fracture edges would produce very high fields and stresses at the fracture line and would be a source of subsequent fractures.

We are starting a numerical modeling effort to simulate emitters being pulled apart by tensile stresses, and the results will be published in a separate paper. One possible scenario would start with a single fragment ejected, leaving sharp fracture lines on both the fragment and the emitter, with the resulting field enhancements producing a series of further fractures and ejected fragments from the emitter. Ionization of these fragments by dark current electrons would produce a conducting path which would short the cavity. The emitter breakup is shown in Fig. 37.

The heating power in the dark current electron beam is equal to $P = IEx$, where I, E, and x are the current, electric field, and gap distance. Currents of ~0.1 mA, a gap distance of 0.1 μm, and electric fields of 1–9 GV/m could deposit mW of power in detached submicron fragments. This is much larger than the $P_\Omega = I^2 \rho dz_e / A_e \sim$ nW of Ohmic heating the material experienced before it was detached, since the electrical resistance of these small fragments would be a few mΩ. The ionization process has been modeled assuming a gas cloud above the emitter site [8], but an evaporating copper fragment would serve the same purpose. While adsorbed gasses could be involved in this process to some degree, the primary ions would be copper, as is seen experimentally [56].

While this mechanism is independent of cavity size or stored energy, the breakdown mechanism seems to deposit a significant fraction of the cavity stored energy locally at the breakdown site, ultimately in melted copper. The size of the stored energy then becomes the determining factor in the volume of copper that is melted.

F. Magnetic field effects

The **B** field can affect emitters in a number of ways. We have shown in the subsection of Sec. III B how $\mathbf{E} \times \mathbf{B}$ drifts affect the emitted current, and how the orbits of emitted electrons follow the **B** field lines. The dominant effect on the surface itself seems to be the Hall effect forces, $\mathbf{F} = \mathbf{I} \times \mathbf{B}$, exerted by the current within the

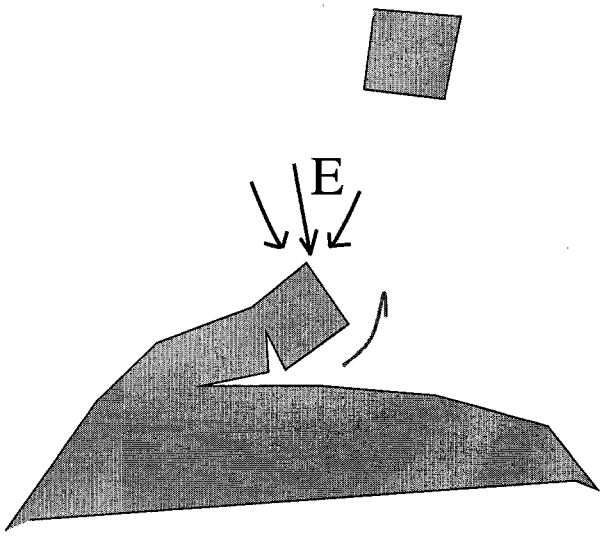

FIG. 37. (Color) Mechanical breakup of an emitter with one fragment gone and another in the process of breaking off.

emitters. Deformation could occur when Hall effect forces exceed the strength of the material; that is when the local Hall pressure, p_H, becomes comparable to the tensile strength of copper, σ_{Cu}, or $p_H = i_{FN}B\sin\theta \sim \sigma_{Cu}$. With a random distribution of emitter angles, θ, relative to the **B** field, $\sin\theta$ is of order 1, and $i_{FN,max} \sim \sigma_{Cu}/B \sim 2 \times 10^8$ A/m^2. As shown in Fig. 4, these current densities are reached and exceeded regularly in normal operation.

We assume that Hall effect forces will physically alter any emitter not aligned with the field and can produce new ones as a result. Conditioning with the field on will alter emitters at angles to the magnetic field and may effectively align the emitters to the field axis. In regions where the **E** and **B** are approximately parallel, there might be very little difference between the behavior with field on and off. In a complex cavity geometry such as the one studied here, the effect of the field would be significant. On the other hand, we would expect the effects of magnetic field on emitters to be much less significant in a cavity geometry with parallel electric and magnetic fields.

VI. MINIMIZING DARK CURRENTS AND BREAKDOWN

There are a number of methods for reducing dark currents in rf cavities. Reducing adsorbed dirt, by cleaning, has been shown to be essential in superconducting rf. Conditioning methods which clean the surface have been shown to be useful. Control of the surface structure with chemical polishing and different methods of turning have also been shown to have a significant effect [57]. The use of different materials may also be desirable, although there is less experimental evidence for this. Harder surfaces should also be better.

The construction of high gradient, low frequency cavities involves considerable stored energy and any breakdown event will deposit much of this energy in a small area of the surface. The subsequent evolution of the cavity probably is more dependent on the parameters of the breakdown event than on the treatment before breakdown. The limits of the control one has over the breakdown process with clean copper surfaces are not well understood.

VII. CONCLUSIONS

We have measured a number of parameters in a multicelled 805 MHz cavity and found that the data are consistent with Fowler-Nordheim field emission from small point sources. Dark current emission seems to take place at local electric fields large enough to produce electrostatic forces sufficient to rip the copper emitters apart, a phenomenon which might be the trigger for breakdown events. We see structures on the inside surface of the cavity which can produce field enhancements of the scale we would expect from dark current measurements. We have presented a cold copper model of breakdown which is consistent with the breakdown we are seeing and with the operation of a wide variety of structures around the world. Our data on dark currents are consistent with a variety of data taken in other accelerating structures which operate from 200 MHz to 11.4 GHz.

The data show the fluxes of dark currents emitted can complicate the design of a single particle muon cooling experiment and we are looking at ways of reducing this flux.

ACKNOWLEDGMENTS

The authors thank S. Geer, T. Kroc, D. Neuffer, A. Rowe, and A. Tollestrup of FNAL, G. Drake and V. Stipp of ANL, R. A. Rimmer and M. Zisman of LBNL, S. Henderson of Cornell, Fermi Media Services, Argonne Radiation Physics, J. Davis of Proxtronics Inc., Springfield, VA, G. Lehr of Kodak, D. Errede of U of IL., R. Edgecock and D. J. S. Findlay of Rutherford Lab, C. Adolphsen and S. Tantawi of SLAC, E. McKigney of Imperial College, and D. Kaplan and H. Li of IIT for their helpfulness. The electron microscopy was carried out in the Electron Microscopy Center at Argonne National Laboratory which is supported by the U.S.D.O.E. Office of Science. This work was supported by the Office of High Energy Physics of the U.S. Department of Energy, at Argonne under Contract No. W-31-109-ENG-38. We would also like to acknowledge the support of the Illinois Board of Higher Education, the Illinois Department of Commerce and Community Affairs, and the NSF.

[1] H. Padamsee, J, Knobloch, and T. Hays, *RF Superconductivity for Accelerators* (John Wiley and Sons, Inc., New York, 1998).

[2] *High Voltage Vacuum Insulation*, edited by R. Latham (Academic Press, London, 1995).

[3] G. A. Mesyats, *Cathode Phenomena in a Vacuum Discharge: The Breakdown, the Spark and the Arc* (Nauka Publishers, Moscow, 2000).

[4] G. A. Mesyats, *Explosive Electron Emission* (URO Press, Ekaterinberg, 1998).

[5] R. L. Boxman, D. M. Sanders, and P. J. Martin, *Handbook of Vacuum Arc Science and Technology, Fundamentals and Applications* (Noyes Publication, Park Ridge, 1995).

[6] *High Energy Density Microwaves, Pajaro Dunes, California, 1998*, edited by R. M. Phillips, AIM Conf. Proc. No. 474 (AIP, New York, 1999).

[7] L. L. Laurent, Ph.D. thesis, University of California–Davis, 2002.

[8] J. Knobloch, Ph.D. thesis, Cornell University, 1997.

[9] Ding Sun, Ph.D. thesis, Texas A&M University, 1992.

[10] http://www-project.slac.stanford.edu/lc/wkshp/RFBreakdwn/references/publist.htm

[11] J. Norem, A. Moretti, and M. Popovic, Nucl. Instrum. Methods Phys. Res., Sect. A **472**, 600 (2001).

[12] V. Wu, Ph.D. thesis, University of Cincinnati, 2002.
[13] A. Moretti, N. Holtkamp, T. Jurgens, and Z. Qian, in *Proceedings of the 20th International Linac Conference, Monterey, CA, 2000*, edited by A. Chao, eConf C000821, THC18.
[14] Study I: A Feasibility Study of a Neutrino Source Based on a Muon Storage Ring, edited by N. Holtkamp and D. Finley, Fermilab, 2000, http://www.fnal.gov/projects/muon_collider/nu/study/report/machine_report/
[15] Feasibility Study-II of a Muon-Based Neutrino Source, edited by S. Ozaki, R. Palmer, M. Zisman, and J. Gallardo, BNL Report No. BNL-52623, 2001, http://www.cap.bnl.gov/mumu/studyii/FS2-report.html
[16] Muon Collider Collaboration, C. M. Ankenbrandt *et al.*, Phys. Rev. ST Accel. Beams **2**, 081001 (1999).
[17] M. A. Green, J. Y. Chen, and S. T. Wang, IEEE Trans. Appl. Supercond. **11**, 2296 (2001).
[18] R. H. Fowler and L. Nordheim, Proc. R. Soc. (London) **A119**, 173 (1928).
[19] R. V. Latham, *High Voltage Vacuum Insulation: The Physical Basis* (Academic Press, London, 1981).
[20] B. Franklin, *Experiments and Observations on Electricity (1774)* (Harvard University Press, Cambridge, 1941).
[21] W. K. H. Panofsky, and M. Phillips, *Classical Electricity and Magnetism* (Addison Wesley Publishing Company, Reading, MA, 1955).
[22] W. P. Dyke and J. K. Trolan, Phys. Rev. **89**, 799 (1953).
[23] S. Dushman, Phys. Rev. **21**, 623 (1923).
[24] Stangenes Industries, Palo Alto, CA, USA.
[25] Tektronix Inc., Beaverton, OR, USA.
[26] Perspective Scientific Limited, W1M 1LA, England.
[27] H. Enge, Rev. Sci. Instrum. **35**, 278 (1964).
[28] H. A. Bethe and J. Ashkin, in *Passage of Radiations Through Matter*, edited by E. Segre, Experimental Nuclear Physics (John Wiley & Sons, Inc., New York, 1953).
[29] Hewlett-Packard, Palo Alto, CA, USA.
[30] M. Reiser, *Theory and Design of Charged Particle Beams* (John Wiley & Sons, Inc., New York, 1994).
[31] S. Humphries, *Charged Particle Beams* (Wiley, New York, 1990).
[32] W. P. Swanson, IAEA Technical Report Series No. 188, 1979.
[33] G. Shani, *Radiation Dosimetry Instrumentation and Methods* (CRC Press, Boca Raton, 1991).
[34] G. Geschonke (private communication).
[35] TESLA Technical Design Report No. 2001-011, 2001.
[36] J. Norem, in *Proceedings of the Workshop on Niobium for rf Cavities, Fermilab, 2002*, http://www-bd.fnal.gov/niobium/talks/norem.pdf
[37] D. J. S. Findlay (private communication).
[38] V. Stipp (private communication).
[39] C. Adolphsen (private communication).
[40] S. Henderson (private communication).
[41] T. Kroc (private communication).
[42] J. W. Wang, SLAC Report No. 339, 1989.
[43] A. Chao and M. Tigner, *Handbook of Accelerator Physics and Engineering* (World Scientific, Singapore, 1999), p. 391.
[44] Central Steel and Wire Company Catalogue, Central Steel and Wire Co., Chicago, IL (2000).
[45] W. P. Dyke, F. M. Charbonnier, R. W. Strayer, R. L. Floyd, J. P. Barbour, and J. K. Trolan, J. Appl. Phys. **31**, 790 (1960).
[46] I. L. Gufel'd, Sov. Phys. Tech. Phys. **17**, 800 (1972).
[47] A. van Oostrom, in *Proceedings of the 6th International Symposium on Discharges and Electrical Insulation in Vacuum, Swansea, 1974* (University College, Swansea, 1974), p. 49.
[48] V. Dolgashev (private communication).
[49] P. Kranjec and L. Ruby, J. Vac. Sci. Technol. **4**, 94 (1964).
[50] I. Brodie, J. Vac. Sci. Technol. **3**, 222 (1966).
[51] E. L. Cook, J. Appl. Phys. **41**, 551 (1970).
[52] J. McPhee, *Rising From the Plains* (Farrar Straus & Giroux, New York, 1986).
[53] B. Bonin, in *Proceedings of the 6th Workshop on RF Superconductivity, 1994*, edited by R. M. Sundelin (CEBAF, Newport News, VA, 1994).
[54] W. D. Kilpatrick, Rev. Sci. Instrum. **28**, 824 (1957).
[55] R. P. Feynman, R. B. Leighton, and M. Sands, *The Feynman Lectures on Physics* (Addison-Wesley, Reading, 1965), Vol. II.
[56] V. A. Dolgashev and S. Tantawi, in *Proceedings of the 9th International Workshop on Linear Colliders* (SLAC, Stanford CA, 2002).
[57] C. Suzuki *et al.*, Nucl. Instrum. Methods Phys. Res., Sect. A **462**, 337 (2001).